JOURNAL OF GEOPHYSICAL RESEARCH, VOL. 104, NO. B1, PAGES 817–844 JANUARY, 1999

Scaling of the shear rupture process from nucleation to dynamic propagation: Implications of geometric irregularity of the rupturing surfaces

Mitiyasu Ohnaka and Lin-feng Shen
Earthquake Prediction Research Center, Earthquake Research Institute, University of Tokyo, Tokyo

Abstract. A series of systematic, high-resolution laboratory experiments have been performed on the nucleation of propagating slip failure on preexisting faults having different surface roughnesses to demonstrate how the size scale and duration of shear rupture nucleation are affected by geometric irregularity of the rupturing surfaces. On the basis of the experimental results it has been discussed theoretically how consistently scale-dependent physical quantities inherent in shear rupture are scaled. The experiments led to conclusive results that the nucleation process consists of two phases (phase I, an initial, quasi-static phase, and phase II, a subsequent accelerating phase) and that the nucleation process is greatly affected by geometric irregularities on the rupturing surfaces. In phase I the rupture grows at a slow, steady speed which is independent of the rupture growth length L. In contrast, during phase II the rupture develops at accelerating speeds V, which increase with an increase in L, obeying a power law $V/V_S = \alpha(L/\lambda_c)^n$, where V_S is the shear wave velocity, λ_c is the characteristic length representing the geometric irregularity of the fault surfaces, and α and n are constants ($\alpha = 8.87 \times 10^{-29}$ and $n = 7.31$). Scale dependency of scale-dependent physical quantities, including the nucleation zone size and its duration, is commonly ascribed to scale dependency of the slip-dependent constitutive law parameter D_c, which is in turn governed by λ_c. It has been discussed that a unified comprehension can be provided for shear rupture of any size scale if the constitutive law for shear rupture is formulated as a slip-dependent law.

1. Introduction

Once shear rupture instability occurs in the brittle regime, the rupture propagates dynamically at a high speed close to sonic velocities. This is often referred to as brittle rupture, and a typical large-scale example is the earthquake rupture instability that takes place in the brittle layer in the Earth's crust. From a physical viewpoint, however, shear rupture cannot begin to propagate abruptly at speeds close to sonic velocities immediately after the instability is attained when the constitutive property of the fault is inhomogeneous. It has been demonstrated by both laboratory experiments [*Dieterich*, 1978; *Dieterich et al*., 1978; *Okubo and Dieterich*, 1984; *Ohnaka et al*., 1986, 1987a; *Ohnaka and Kuwahara*, 1990; *Ohnaka*, 1990, 1996; *Kato et al*., 1992] and numerical simulations [*Yamashita and Ohnaka*, 1991; *Matsu'ura et al*., 1992; *Dieterich*, 1992; *Dieterich and Kilgore*, 1996; *Rice and Ben-Zion*, 1996; *Tullis*, 1996; *Kato and Hirasawa*, 1997; *Shibazaki and Matsu'ura*, 1998] based on constitutive laws for friction or shear rupture that unstable, high-speed rupture is preceded by stable, quasi-static rupture growth in a localized zone. The transition process from stable, quasi-static rupture growth to the phase of unstable, high-speed rupture in a localized zone is what is called the nucleation process.

High-resolution laboratory experiments on propagating mode II type shear rupture along a preexisting fault have suggested [*Kuwahara et al*., 1986; *Ohnaka*, 1996] that the nucleation process consists of two phases: phase I is an initial, quasi-static phase, and phase II is the subsequent accelerating phase, which eventually leads to dynamic high-speed propagation of the rupture. However, understanding the nucleation process of shear rupture quantitatively in terms of the underlying physics is still far from complete. It has widely been recognized that some physical quantities inherent in shear rupture are scale-dependent. For instance, recent studies [*Ohnaka*, 1996, 1998] suggest that the size of shear rupture nucleation and its duration are scale-dependent; that is, the size scale and duration of the nucleation increase with an increase in the characteristic length representing the fault surface roughness. If this is the case, both the critical size of nucleation and its duration for large-scale earthquake rupture should differ greatly from those for shear rupture of small scale in the laboratory. However, how these scale-dependent physical quantities are scaled in terms of the underlying physics remains unresolved. More specifically, by what physical parameter are these scale-dependent quantities scaled consistently in quantitative terms? These unresolved problems are critical to provide a unified comprehension for shear rupture of any size scale, from small scale in the laboratory to large scale in the Earth as an earthquake source.

During shear rupture, slip displacement proceeds on the rupturing surfaces in the breakdown zone behind the propagating front of rupture, and hence the rupturing surfaces are in mutual contact and are interacting throughout the breakdown process. This suggests that the shear rupture process may be severely affected by geometric irregularities on the rupturing surfaces and that the size of the breakdown zone over which the shear strength degrades transitionally to a residual friction

Paper number 1998JB900007.
0148-0227/99/1998JB900007$09.00

stress level with ongoing slip may also be greatly influenced by these geometric irregularities. This leads to the speculation that geometric irregularities on the rupturing surfaces will be a key factor in scaling the size scale and duration of the shear rupture process.

In this paper we first wish to demonstrate with laboratory experiments how severely the length scale of shear rupture nucleation is affected by geometric irregularities on the rupturing surfaces and then to show theoretically how the critical length of the nucleation zone and its duration are scaled consistently by a characteristic scale representing the geometric irregularity of the fault zone. To this end, we have conducted a series of specifically designed, systematic, high-resolution laboratory experiments, which will be described in sections 3 and 4. On the basis of experimental results, in terms of the constitutive law for shear rupture from the theoretical viewpoint, we finally discuss the idea that a characteristic scale representing the geometric irregularity of the fault zone plays a critical role in scaling scale-dependent physical quantities inherent in shear rupture.

2. A Characteristic Scale Representing Geometric Irregularity of the Fault Surfaces

The earthquake source at crustal depths is an unstable, dynamically propagating shear rupture along a plane or zone of weakness (referred to as a preexisting fault). The geometry of a fault (such as bends, stepovers, and bifurcations) and the fault zone structure (such as the topographic irregularity of the fault surfaces and the presence of fault gouge) play important roles in the process of earthquake generation because such geometric structure and/or irregularity substantially prescribe(s) the mechanical heterogeneity of the fault, which in turn controls the earthquake generation process.

A typical example of such geometric structure and/or irregularity of the fault (zone) may be a local patch of high rupture growth resistance on faults [*Ohnaka*, 1998]. There is strong circumstantial evidence that an “asperity” [*Kanamori and Stewart*, 1978; *Kanamori*, 1981] or “barrier” [*Aki*, 1979, 1984] on earthquake faults is a local patch of high rupture growth resistance whose strength equals the strength of intact rock at lithospheric conditions [*Ohnaka et al.*, 1997; *Ohnaka*, 1996, 1998], and such a high rupture growth resistance will be attained at portions of fault bend or stepover, at interlocking asperities on the fault surfaces with topographic irregularity, and/or at portions of adhesion (or cohesion) healed between the mating fault surfaces during the interseismic period. If this is the case, the size of a local patch of high rupture growth resistance on an earthquake fault provides a characteristic length (or distance) representing the geometric property of the fault (zone). Other characteristic lengths (or distances) representing geometric properties of earthquake faults include fault zone thickness, fault segment size, and the depth of seismogenic layer [e.g., see *Aki*, 1996; *Knopoff*, 1996]. The earthquake generation process and its eventual size are necessarily characterized by these macroscopic length scales [*Sibson*, 1984; *Scholz*, 1982, 1994; *Romanowicz*, 1992; *Aki*, 1996; *Knopoff*, 1996; *Matsu'ura and Sato*, 1997]. Of these characteristic scales, focus is placed in this paper on a characteristic scale of the order of the amount of slip required for the slipping zone behind the moving front of rupture to break down.

As mentioned in section 1, the rupturing surfaces during the breakdown process of shear rupture are in mutual contact and interacting, so that the shear rupture process is likely affected by geometric irregularities on these rupturing surfaces. This suggests that the characteristic length representing the topographic irregularity of the rupturing surfaces may be a key to scaling scale-dependent physical quantities inherent in shear rupture. To investigate this, we have conducted a series of laboratory experiments on propagating shear rupture of mode II type, focusing on the role of geometric irregularity of the fault surfaces in scaling the nucleation zone size and its duration.

The aim of the laboratory experiments was to test how the shear rupture process is affected by geometric irregularity of the fault surfaces. To this end, faults with different surface topographies (or roughnesses) were prepared by lapping the flat (ground) surfaces with carborundum grit having different grain sizes, in the range from coarse grit (#60, representative particle sizes of 210–250 μm) to fine grit (#2000, representative particle sizes of 7–9 μm). The profiles of these fault surfaces were measured with a diamond stylus profilometer with the tip radius of 2 μm, and the resolution of the elevation data collected was 0.0084 μm. The fault surface topographies prepared with grits #60, #600, and #2000 are hereafter referred to as rough, smooth, and extremely smooth faults, respectively, and the three-dimensional (3-D) surface profiles of the faults with these three representative topographic irregularities are shown in Figure 1 for comparison.

Figures 2a and 2b show plots of the logarithm of the topographical length $L(r)$ against the logarithm of the ruler length r for the three representative examples of the fault surfaces with different roughnesses shown in Figure 1. $L(r)$ in Figure 2 has been measured with a ruler length r along the slip direction on the fault surfaces. We find from Figure 2 that the relation between $\log L(r)$ and $\log r$ can be represented by segments of linear line with different slopes, suggesting that the surface roughnesses of the faults shown in Figure 1 exhibit band-limited self-similarity. If this is the case, the relation between $L(r)$ and r within each bandwidth can be expressed by the power law:

$$L(r) = A_i r^{-a_i} \qquad \lambda_{ci-1} < r < \lambda_{ci} \tag{1}$$

where A_i and a_i are constants in a bandwidth bounded by lower corner length λ_{ci-1} and upper corner length λ_{ci} ($i = 1, 2, \cdots, k$). The corner length λ_{ci} is defined here as the length that separates the neighboring two bands with different segment slopes a_i and a_{i+1}. Note that a corner length thus defined is a characteristic length representing the fault surface irregularity. Fault surface topographies may, in general, be quantified and characterized in terms of these two parameters: a_i and λ_{ci}.

Specifically, for instance, the parameters characterizing the fault surface roughnesses shown in Figure 1 have been evaluated from the data shown in Figure 2; that is, $\lambda_{c1} = 10^{1.83} = 67.6$ μm, $\lambda_{c2} = 10^{2.3} = 199.5$ μm, $a_1 = 0.0229$, and $a_2 = 0.0085$ for the rough surface (grit #60); $\lambda_{c1} = 10^{1.25} = 17.8$ μm, $\lambda_{c2} = 10^{1.66} = 45.7$ μm, $a_1 = 0.0076$, and $a_2 = 0.0028$ for the smooth surface (grit #600); and $\lambda_c = 10^1 = 10$ μm, and $a = 0.0017$ for the extremely smooth surface (grit #2000). These values for λ_{ci} suggest that λ_{ci} is primarily characterized by grain size of carborundum grit used for lapping the fault surfaces.

We thus conclude that the fault surface roughnesses prepared for the present experiments can be characterized in terms of the parameters a_i and λ_{ci}. Of these two parameters, however, only the corner length λ_{ci} straightforwardly repre-

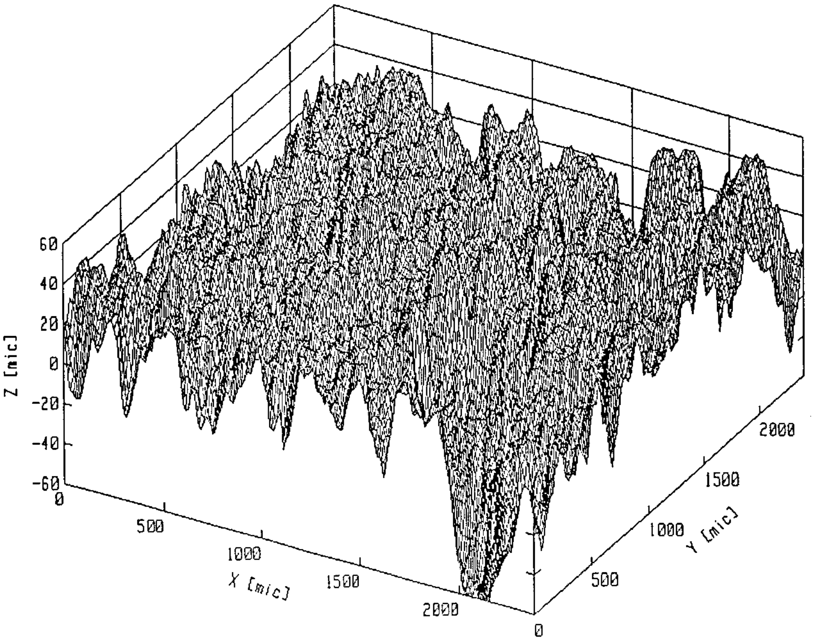

Rough fault surface

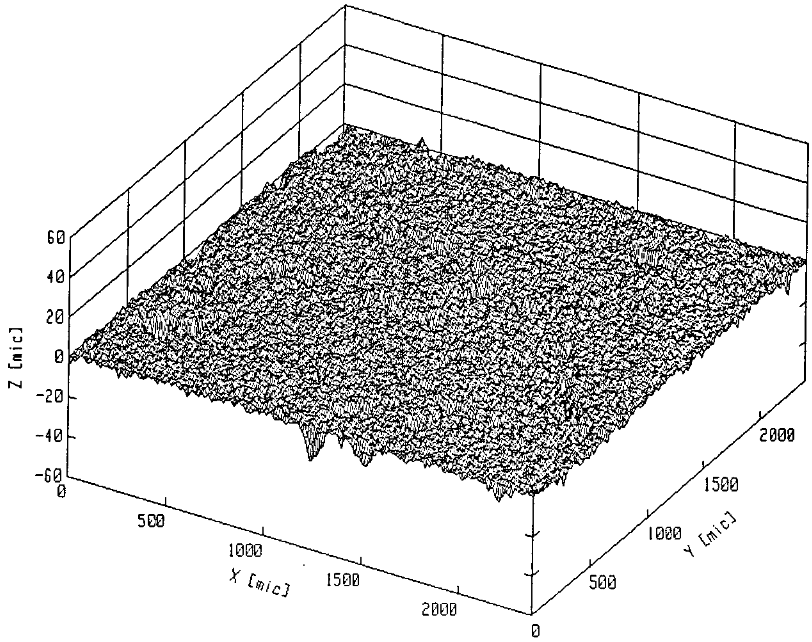

Smooth fault surface

Figure 1. Three representative examples of the profiles of fault surface topographies: rough, smooth, and extremely smooth surfaces. The rough fault surface was prepared with grit #60, the smooth fault surface was prepared with grit #600, and the extremely smooth fault surface was prepared with grit #2000.

sents a characteristic length scale in the slip direction on the fault, and hence attention will hereafter be paid to λ_{ci} alone. Some of the values estimated here for λ_{ci} will be used in a later analysis (sections 4 and 5). We will see later that λ_{ci}, in fact, plays a critical role in scaling the size and duration of shear rupture nucleation.

3. Experimental Method

Tsukuba granite from Ibaraki Prefecture, central Japan, was selected for the present experiments. The granite is fairly fine grained and has been used in previous experiments on propagating slip failure of stick slip [*Ohnaka et al.*, 1986, 1987a, b;

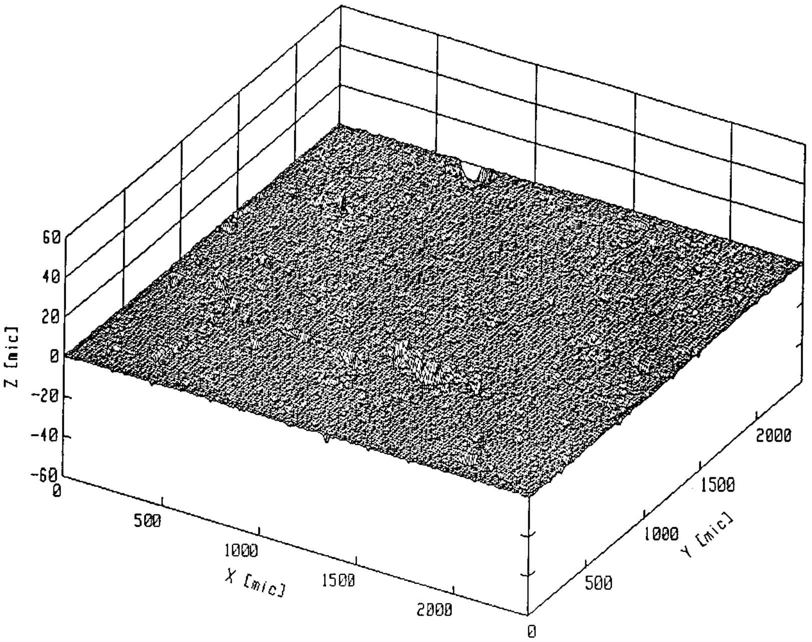

Extremely smooth fault surface

Figure 1. (continued)

Ohnaka and Yamashita, 1989; *Ohnaka and Kuwahara*, 1990; *Ohnaka*, 1996]. Physical parameters for this rock at room temperature and atmospheric pressure are as follows: the rigidity is 2×10^4 MPa, Poisson's ratio is 0.12, the longitudinal wave velocity is 4.4 km/s, and the shear wave velocity is 2.9 km/s. Three blocks of this granite with planar and parallel faces were prepared for the present experiments; one block (labeled A) has dimensions of 250 × 290 × 50 mm, and the other two blocks (labeled B and C) have dimensions of 100 × 290 × 50 mm. These block surfaces were ground flat with a reciprocating surface grinder to an accuracy of less than 0.02 mm per 1 cm length.

The configuration for the present experiments was a double-direct-shear failure test of mode II type along the two parallel

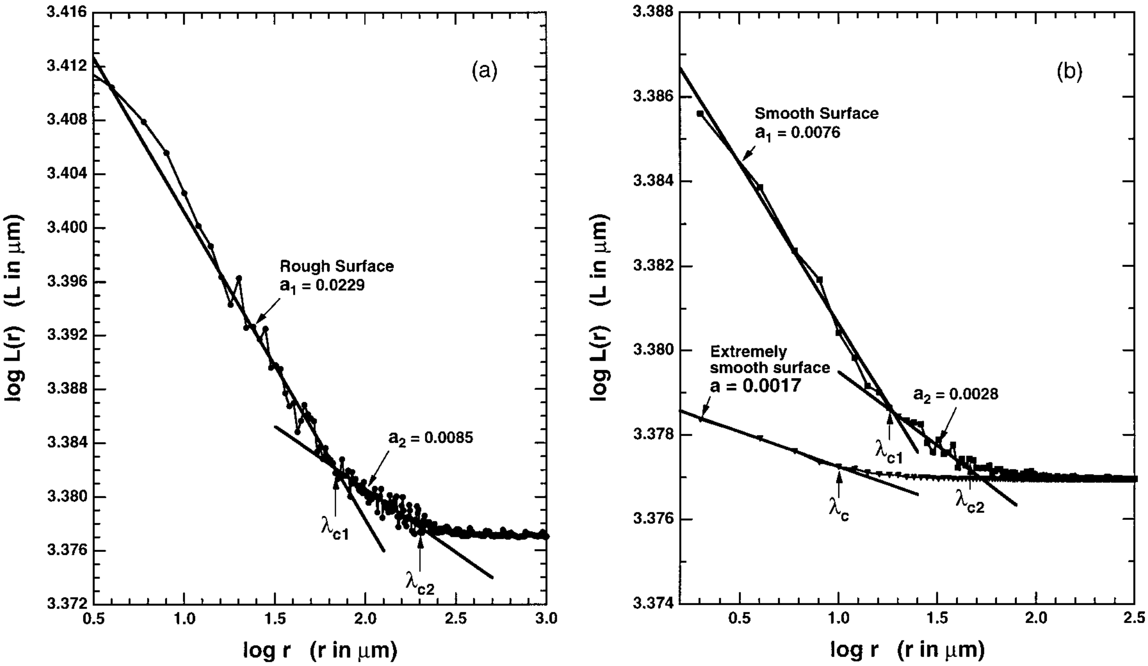

Figure 2. Plots of the logarithm of the topographical length $L(r)$ against the logarithm of the ruler length r (a) for a rough fault surface and (b) for smooth and extremely smooth fault surfaces shown in Figure 1.

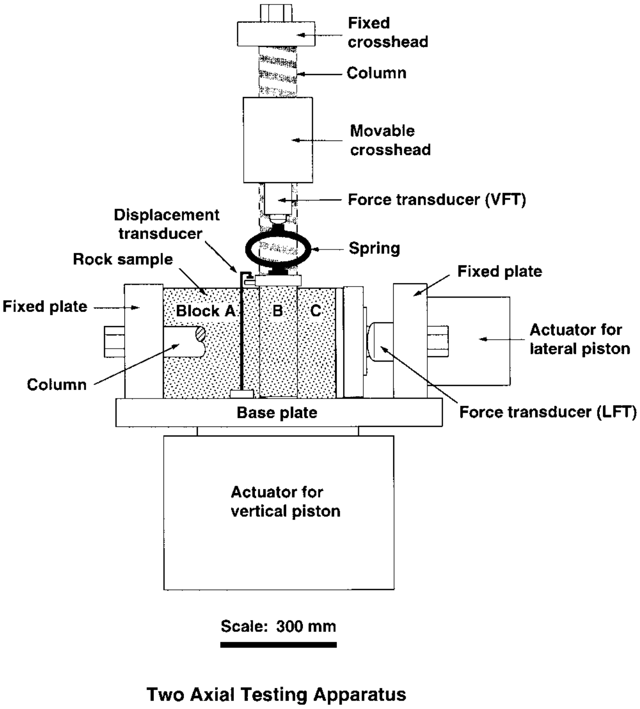

Figure 3. The configuration for the present experiments.

preexisting faults (Figure 3), in which the 290 mm long and 50 mm wide mating surfaces act as weak junctions under an applied normal load. The load normal to the fault surfaces is first applied by a horizontal ram which is servo-controlled to be held constant. The tangential force on the plane of the fault surfaces is then applied, independent of the normal force across the fault surfaces, by a vertical ram, to push the inner block B between the two other blocks A and C (see Figure 3). The shear load application was servo-controlled such that the sample was deformed at a constant rate of 6.7×10^{-4} mm/s throughout the experiments, unless otherwise stated. The sample deformation was measured with a displacement transducer mounted at the position shown in Figure 3. The normal load and shear load were measured directly with force transducers (Figure 3). The stiffness of the vertical loading system was 5×10^6 N/cm. This loading system stiffness was lowered to 6×10^5 N/cm by using the oval spring (Figure 3). The loading system with the oval spring was used in the experiments for faults having the rough or smooth surfaces.

The shear load application necessarily leads to the accumulation of shear stresses along the two parallel faults, and this eventually results in the onset of shear rupture nucleation of mode II type on either of the two faults. In the present experiments, blocks B and C were simply utilized as auxiliaries to bring about shear stress along the fault between blocks A and B, so that here we analyze the events of shear failure that began to nucleate first only on the fault between blocks A and B. This is because our primary interest is in investigating physical process of shear rupture nucleation that is not contaminated by the effect of (parallel) fault-fault interaction, although the effect of fault-fault interaction itself deserves investigation.

To get constitutive information on how the local strength in the breakdown zone behind the rupturing front progressively degrades with ongoing local slip, a series of semiconductor strain gauges, with active gauge length of 2 mm, were mounted on block A at 25 mm intervals along the fault between blocks A and B and at positions 5 mm from the fault; 12 pairs of strain gauges with mutually perpendicular orientations were used to monitor local shear strains in the direction parallel to the fault (S1 to S12 in Figure 4a). The local shear stresses along the fault were evaluated by multiplying these local shear strains by the rigidity μ of the granite sample. The deployment of the series

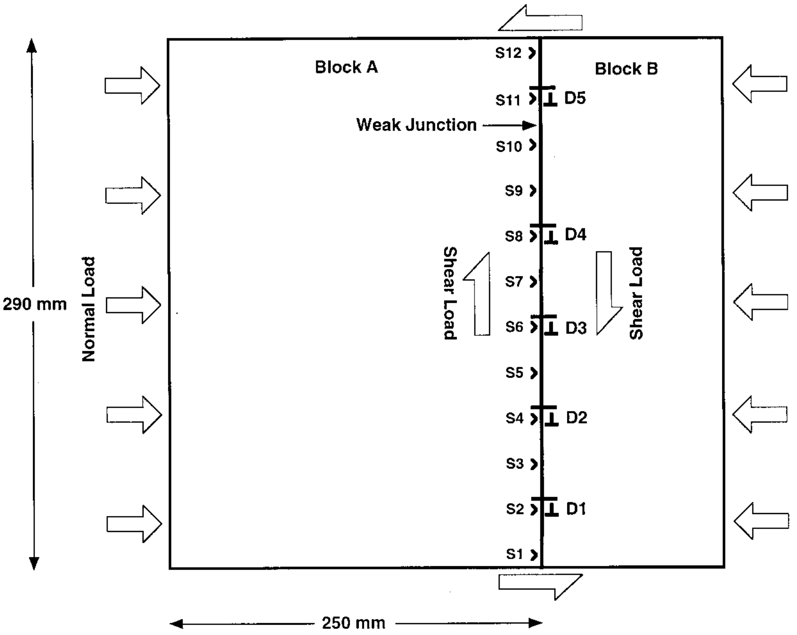

Figure 4a. Sample configuration with two types of sensors in position. S1 to S12 denote the positions at which 12 pairs of strain gauges were mounted to measure local shear strains in the direction parallel to the fault, and D1 to D5 denote the positions at which displacement sensors were mounted to measure local slips on the fault.

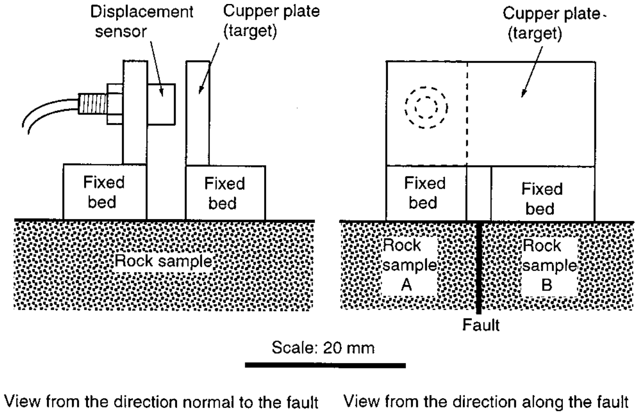

Figure 4b. Setup of the displacement transducer of eddy current loss type in the present experiments.

of 12 shear strain sensors along the fault enabled us to observe how shear rupture nucleates on the fault.

Frequency characteristics of a semiconductor strain gauge sensor mounted on the sample block are determined by (1) frequency response of the semiconductor crystal used, (2) the cementing technique, and (3) the relation between the gauge length and the wavelength of the signals [*Ohnaka et al.*, 1983, 1986, 1987b]. The theoretical limitation of the frequency response of the semiconductor crystal ($>10^5$ MHz) is much higher than the frequency range of signals of present concern (<1 MHz). Hence the limitation of the frequency response of the crystal does not need to be considered. In the present experiments, strain gauges were cemented with α-cyanoacrylate cement with great care. Creep of this cement is negligible for the timescale of the present experiments. Frequency characteristics of the strain gauge sensor therefore are practically determined by the relation between the gauge length and the wavelength of the signals alone. In other words, the strain gauge sensor functions as a kind of low-pass filter, and the cutoff frequency is prescribed by the relation between the gauge length and the wavelength of signals.

The transfer function $f(\Delta X)$ of a strain gauge sensor with effective length L is given by [*Ohnaka et al.*, 1983, 1986, 1987b]

$$f(\Delta X) = \frac{\sin(\pi \Delta X)}{\pi \Delta X} \tag{2}$$

where $\Delta X = (fL \cos\theta)/c$. Here θ is the angle between the direction of the gauge length and the direction of the signal propagation, c is the propagation velocity of the signal, f is the signal frequency, and the signal has been assumed to be plane waves. When the propagation direction of a signal is parallel to the direction of the gauge length, frequency response of a strain gauge sensor with a gauge length of 2 mm is flat from DC to 520 kHz (−1.8 dB), if the propagation velocity of the signal is assumed to be 3 km/s [*Ohnaka et al.*, 1983, 1986, 1987b]. This shows that the use of a strain gauge with effective length of 2 mm as a sensor to measure local shear strain is sufficient for the present purpose.

Local slip displacements between the two sides of the fault are also required for investigating constitutive properties in the breakdown zone behind the propagating front of shear rupture. To measure local slips on the fault, two types of sensors were used: displacement transducer of eddy current loss type (DTEC), and metallic foil strain gauge (MFSG). Local slip displacements, unless otherwise stated, were measured at five positions along the fault (D1 to D5 in Figure 4a).

The displacement transducer of eddy current loss type utilizes the principle that a change in the distance between the sensor and the corresponding metal target is uniquely converted to a change in the inductance of the sensor coil to which high-frequency electric current has been supplied. The inductance change is converted to a change in the output voltage which are recorded. A copper plate has been selected here as the metal target. The shape of the commercially available sensor was circular (3 mmϕ × 5 mm), and the sensor and target plate were mounted with epoxy resin on the granite sample surface, as shown in Figure 4b. The output frequency response of this displacement measuring system including the sensor, amplifier, and linealizer was flat from DC to 20 kHz (−3 dB). The accuracy and resolution of these data are within 2.9×10^{-4} mm. Displacement sensors of this type were used in most of the experiments on slip failure generated on the rough and smooth faults.

Stick-slip failure on a fault with the extremely smooth surfaces occurs more violently than stick slip on the smooth and rough faults, when other conditions are equal. This suggests that local slip displacements during slip failure on the extremely smooth fault move more quickly, which may possibly contain frequency components significantly higher than 20 kHz. Hence the displacement sensor of eddy current loss type was not used for measuring local slip displacements during stick-slip failure on the extremely smooth fault. Instead, metallic foil strain gauges with active gauge length of 2 mm were used as the displacement transducer in this series of experiments. High stiffness of the loading apparatus reduces the amount of slip during a stick-slip failure, so that the loading system without the oval spring was employed in the stick-slip experiments on the extremely smooth fault (Figure 3). This made it possible to measure local slips during a stick-slip failure directly with metallic foil strain gauges.

How to measure a local slip between the two blocks with a metallic foil strain gauge is illustrated in Figure 4c. The deformation (dL/L) of a strain gauge sensor with active gauge

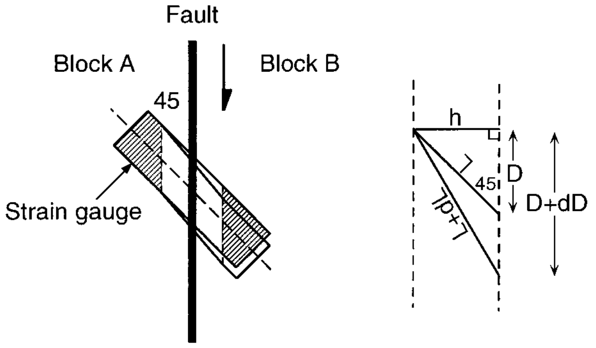

Figure 4c. Illustration of how to measure a local slip between two blocks A and B with a strain gauge. Hatched portions indicate cemented area. A strain gauge is cemented with α-cyano-acrylate cement such that the strain gauge makes an angle of 45° with respect to the direction of fault length. L and $L + dL$ indicate active gauge lengths before and after slip, respectively, and D and $D + dD$ indicate their components in the slip direction before and after slip, respectively. $D = h = L/\sqrt{2}$.

length L is converted to the amount of slip (dD) on the fault by

$$\begin{aligned} dD &= \sqrt{(L + dL)^2 - h^2} - D \\ &= h(\sqrt{2(1 + dL/L)^2 - 1} - 1) \\ &\approx h\left(2\frac{dL}{L}\right) = \sqrt{2}L\frac{dL}{L} \end{aligned} \tag{3}$$

Equation (3) shows that the maximum amount of measurable slip is limited by the maximum durable deformation of a strain gauge used; for instance, when $L = 2$ mm, $dD = 2.8$ μm for $dL/L = 10^{-3}$ and $dD = 28$ μm for $dL/L = 10^{-2}$. This technique therefore has a disadvantage that strain gauge sensors must be renewed every several consecutive stick-slip failures. Nevertheless, this technique has been used in previous experiments [*Ohnaka et al.*, 1986, 1987b; *Ohnaka and Yamashita*, 1989; *Ohnaka and Kuwahara*, 1990] to measure dynamic local slips on the fault, because it has a high sensitivity (10^{-2} μm), and flat frequency response from DC to a frequency higher than 100 kHz.

Figure 4a shows the relation between the fault and the positions of the series of measuring sensors for both local shear strain and slip displacement along the fault. In the experiments on slip failure generated on the rough fault, amplified signals of these local shear strains and slip displacements along the fault, signals of the shear and normal loads remotely applied, and the overall deformation between both ends of the sample blocks A and B along the fault, were sampled at a preset frequency of 500 Hz synchronized by a single clock, with a multichannel analog-to-digital converter with 14-bit resolution. In the experiments on slip failure on the smooth fault, all the amplified analog signals were bifurcated, and one set of bifurcated signals was sampled at a frequency of 500 Hz, with the multichannel analog-to-digital converter with 14-bit resolution, and the other set of the signals was sampled at a frequency of 1 MHz, with another multichannel analog-to-digital converter with 12-bit resolution. In the experiments on slip failure on the extremely smooth fault the amplified signals were sampled at a frequency of 1 MHz, with the multichannel analog-to-digital converter with 12-bit resolution. The overall response of the entire measuring and recording system was flat from DC to 200 kHz for the local shear strain signals, DC to 20 kHz (when DTEC sensors were used) or DC to 100 kHz (when MFSG sensors were used) for the displacement signals, and DC to 2 kHz for the remotely applied shear and normal load signals.

4. Experimental Observations

4.1. Nucleation Phases Developed Along Faults With Different Surface Roughnesses

4.1.1. Rough fault. When shear load is applied with the vertical ram along the fault at a constant rate, while the load normal to the fault has been held constant, the shear stress along the fault begins to build up. Figure 5 shows an example of recorded data on shear failure developed on the rough fault. In Figure 5 the shear load, which is the output signal from force transducer (VFT in Figure 3), and the relative displacement measured between both ends of the sample blocks A and B along the fault are plotted against time. In this experiment the shear load was applied at a constant deformation rate of 6.7×10^{-4} mm/s at the normal load of 6.2 MPa. The origin of time t has been set such that $t = 0$ when the shear load was applied.

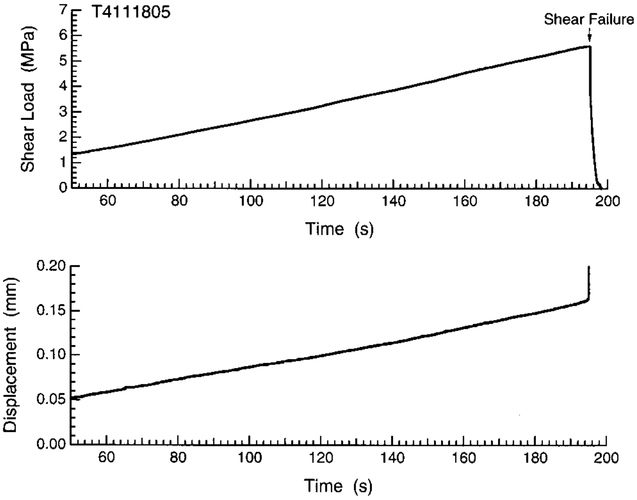

Figure 5. An example (event T4111805) of time records of remotely applied shear load and the relative displacement between both ends of the sample blocks A and B for a slip failure event on the rough fault.

Figure 5 shows that the remotely applied shear load increased with time at the constant rate until shear failure occurred at the time of $t = 195.08$ s, and no strength degradation or slip acceleration preceding overall shear failure is discernible from Figure 5. However, shear stresses monitored at a series of different positions along the fault show how nonuniformly the local shear stresses are induced and accumulated along the fault during shear load application and how gradually the fault strength degrades in a localized zone prior to the eventual, overall failure. This is investigated in detail below.

Figure 6 shows how local shear stresses were induced along the fault and built up with time during the process where the shear load was remotely applied at the constant rate of deformation (6.7×10^{-4} mm/s). Figure 6 shows the data for the same failure event shown in Figure 5. The local shear strains were measured at 12 positions (S1 to S12) along the fault (see Figure 4a), and the local shear stresses were evaluated by multiplying these local shear strains by the rigidity of the granite sample. Differential shear stress (τ_{d0}) in Figure 6 has been defined by

$$\tau_{d0} = \tau - \tau_{t0} \tag{4}$$

where τ represents a local shear stress measured at a position along the fault and τ_{t0} represents the initial local shear stress induced at the same position when the normal load was remotely applied before the shear load application. Note that the initial shear stress τ_{t0} is not necessarily nought (see Figure 7) because shear stress can be induced locally by application of normal load on a fault with topographic irregularities. Thus the differential shear stress τ_{d0} defined by (4) is the net local shear stress at a position along the fault accumulated during shear load application.

It has been found in this series of experiments that nonuniform distribution of shear stress is inevitably induced and developed along the fault, although the normal and shear loads have been remotely applied uniformly (see Figure 6). We postulate that this is because the fault has topographic irregularity

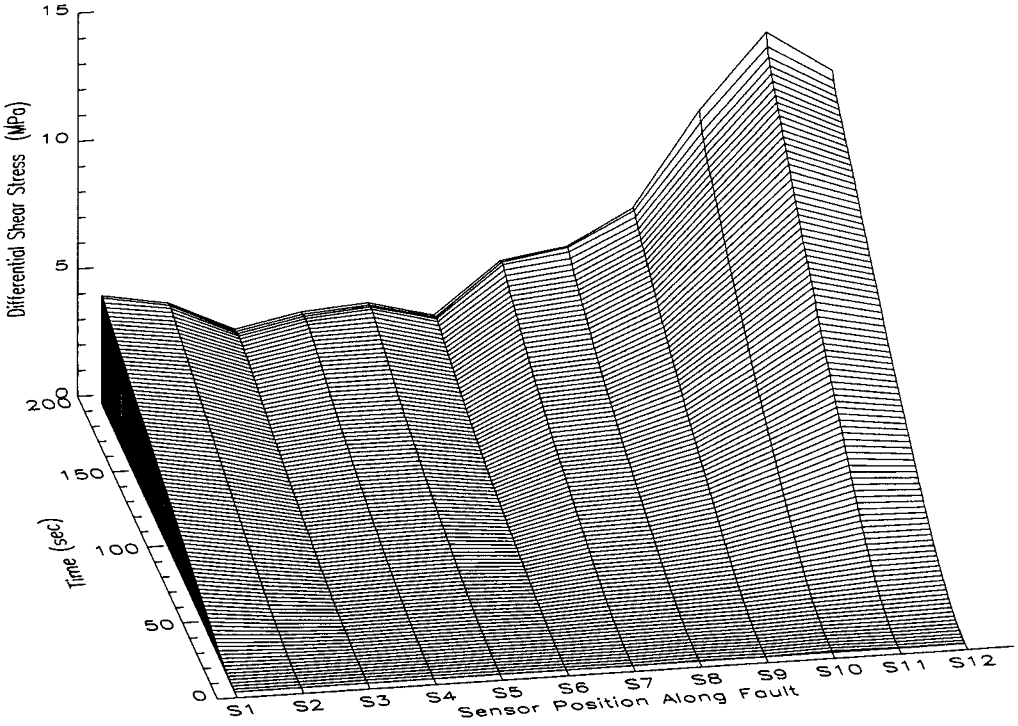

Figure 6. Time and spatial variations of differential shear stresses (τ_{d0}) recorded locally at 12 positions along the fault for the slip failure event shown in Figure 5 (rough fault).

on the surfaces; in other words, nonuniform distribution of the stress developed along the fault is a manifestation of the topographic irregularity of the fault surfaces.

How nonuniformly shear stress was induced and accumulated along the fault with time during shear load application may be more clearly seen in Figure 7. Data in Figure 7 are the same for the failure event shown in Figure 6. The top thick line in Figure 7 represents the distribution of the peak shear strength τ_p along the fault. The peak shear strength is defined as the maximum shear strength during the local breakdown process behind a propagating rupture front at a position on the fault. The bottom thick line represents nonuniform distribution of the initial shear stress, which was induced by application of the normal load of 6.2 MPa. Positive and negative shear stresses in Figure 7 indicate clockwise and anticlockwise shear, respectively. A series of thin lines in Figure 7 indicates levels of local shear stresses accumulated with time on the fault, and these local stress levels are plotted at 19.2-s intervals from t = 3.86 s after the shear load application. It is clearly seen from Figure 7 how nonuniformly the fault strength and the shear stress are distributed along the fault and that the higher the local strength at a position on the fault, the higher is the rate of the shear stress accumulation at the position during shear load application. This observation suggests that the strength distribution along a fault could be inferred from the stress distribution along the fault, or vice versa, because of a strong correlation between the two.

Shear stress concentrates more where the fault strength is locally higher. However, shear failure, in general, begins to nucleate around the location where the strength is the lowest (Figures 7 and 8). This has also commonly been observed in the present series of experiments. In the experiment on the failure event in Figures 5–7, the overall failure occurred at t = 195.08 s; however, the nucleation phase for this event is not significantly discernible from Figures 5–7. This is because the amount of stress degradation and slip for the nucleation is very small compared with that for the overall failure event.

Figure 8 illustrates the degradation of shear stress associated with rupture nucleation along the fault on enlarged scales of

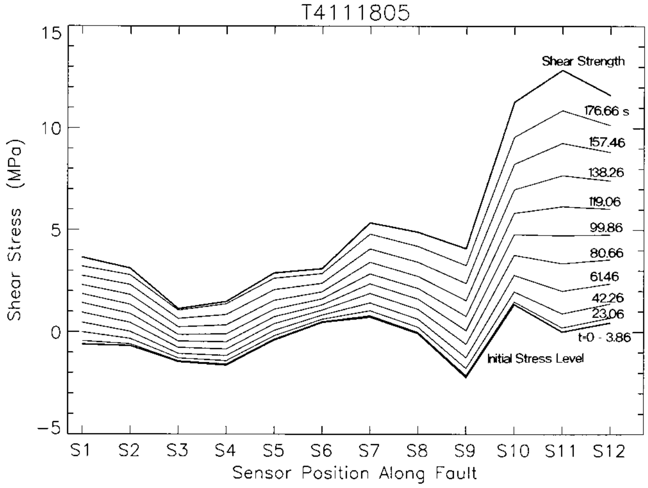

Figure 7. Nonuniform distributions of the fault strength (top thick line), initial shear stress level (bottom thick line) induced by application of the normal load (6.2 MPa), and variations of levels of local shear stresses along the fault with time for the slip failure event shown in Figures 5 and 6 (rough fault) for event T4111805. Local shear stress levels are plotted at 19.2-s intervals from t = 3.86 s after shear load application. Positive or negative shear stress indicates clockwise or anticlockwise shear, respectively.

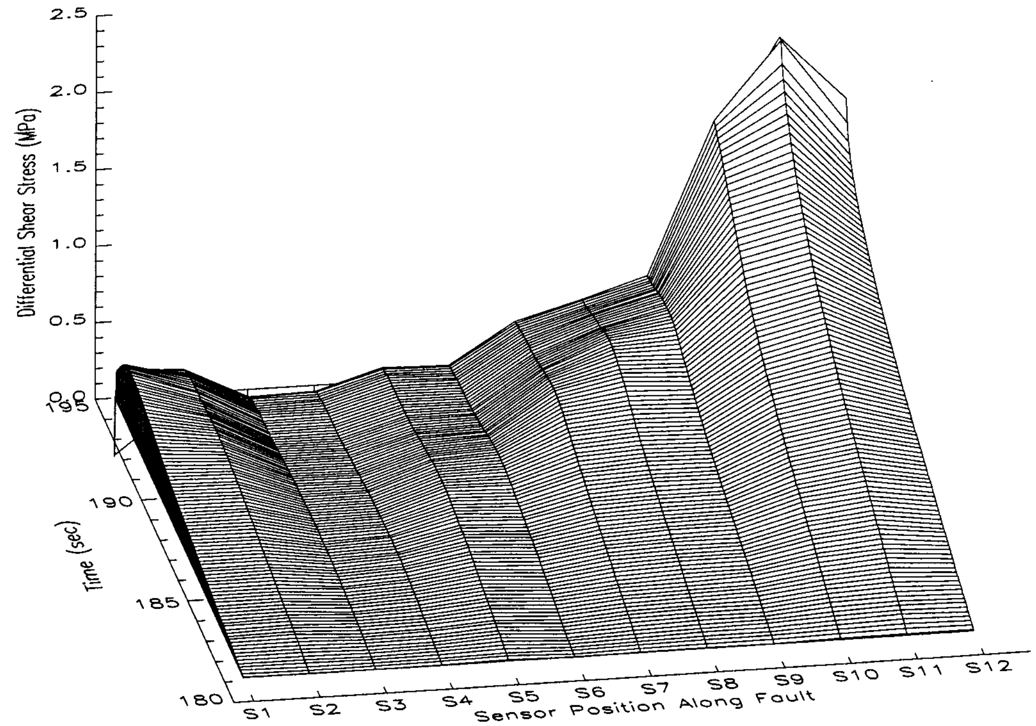

Figure 8. Time and spatial variations of differential shear stresses (τ_{d180}) recorded locally at 12 positions along the fault during the nucleation for the failure event shown in Figures 5–7 (rough fault).

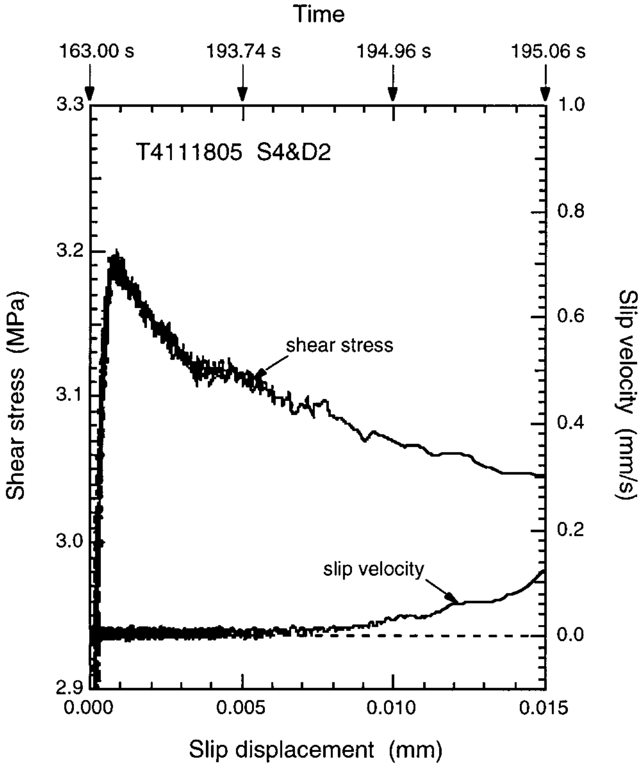

Figure 9. A plot of the shear stress measured at S4 against the slip displacement at the same position (D2) during the nucleation for the failure event (T4111805) shown in Figures 5–8 (rough fault). The slip velocity is also plotted against the slip displacement. The time axis is added to facilitate comparison with Figures 8, 20a, 20b, and 21.

the stress and time axes. Differential shear stress (τ_{d180}) in Figure 8 has been defined by

$$\tau_{\mathrm{d180}} = \tau - \tau_{\mathrm{t180}} \tag{5}$$

where τ represents a local shear stress at a time t recorded at a position along the fault and τ_{t180} represents the local shear stress at $t = 180$ s, recorded at the same position. Figure 8 allows one to identify the position from which shear rupture began to nucleate and how the nucleation developed with time.

It is found from Figure 8 that local shear stresses at nine positions (S1 through S9) along the fault decreased gradually with time, after they had attained peak values (peak shear strength τ_{p}) at these individual positions. A gradual decrease in local shear stress at a position suggests that the rupture has begun to occur stably and slowly at the position. Shear rupture is defined, in terms of fracture mechanics, as the process during which the shear strength degrades to a residual friction stress level with ongoing slip displacement on the rupturing surfaces. Therefore, whether or not shear rupture has indeed occurred at a position of shear stress degradation can be checked by observing the slip-weakening relation at that position.

An observed slip-weakening relation for the failure event shown in Figure 8 is exemplified in Figure 9. Figure 9 is a plot of the shear stress measured at S4 against the slip displacement measured at the same position (D2) (see Figure 4a) during the nucleation for this particular event. Figure 9 demonstrates that shear rupture has actually proceeded locally at a position of shear stress degradation on the fault. We can thus conclude from Figure 8 that shear rupture began to nucleate roughly at $t = 185$ s somewhere around positions S3 and S4 on the fault and that the rupture grew slowly and bidirectionally along the fault. Slow extension of a localized slip-weakening zone along

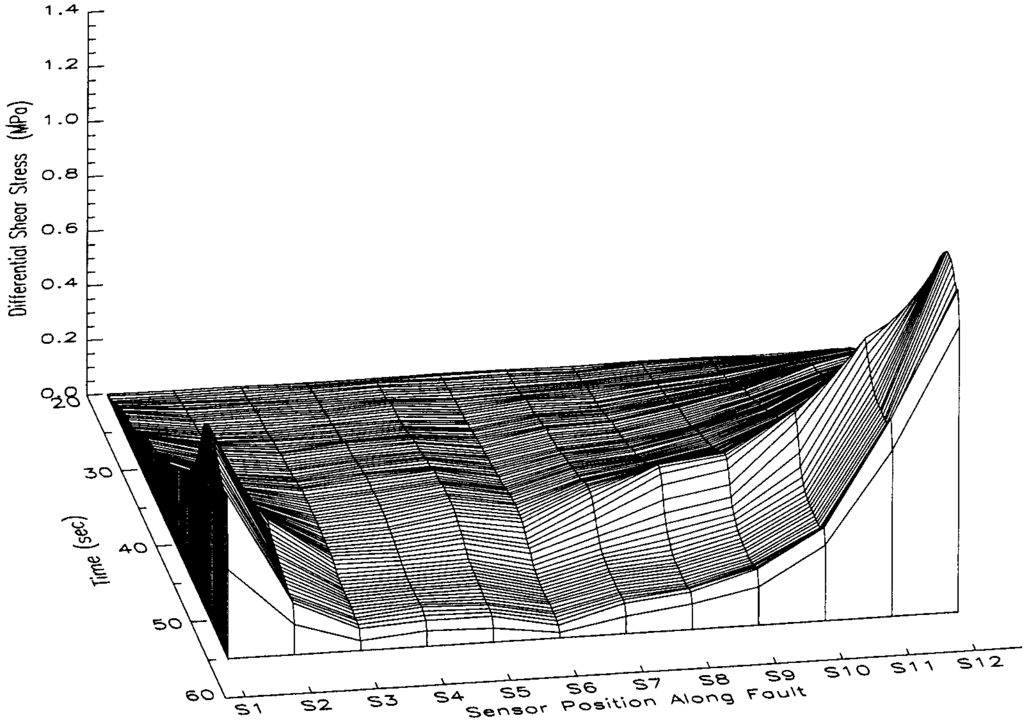

Figure 10. Time and spatial variations of differential shear stresses (τ_{d20}) recorded locally at 12 positions along the fault during the nucleation for another slip failure event on the rough fault.

the fault with time (see Figure 8), prior to unstable, overall shear rupture at $t = 195.08$ s, is what has been referred to as the rupture nucleation, which is an integral part of unstable, dynamic rupture.

Another example of the nucleation phase of a different slip failure that developed on the same rough fault is shown in Figure 10 to demonstrate the reproducibility. In this experiment, the shear load was applied at a constant rate of 2.2×10^{-4} mm/s at the normal load of 6.2 MPa. Differential shear stress (τ_{d20}) in Figure 10 has been defined by

$$\tau_{d20} = \tau - \tau_{t20} \qquad (6)$$

where τ represents a local shear stress at a time t at a position along the fault and τ_{t20} represents the local shear stress at $t = 20$ s recorded at the same position, and the origin of time t has been taken arbitrarily in Figure 10. As the nucleation phase is viewed from the rear in Figure 10, one can see from Figure 10 how transitionally the nucleation phase develops to overall rupture of the preexisting fault. An observed slip-weakening relation at position S6 along the fault for this nucleation phase is shown in Figure 11 to demonstrate that shear rupture has indeed occurred at a position of stress degradation. The slip-weakening curves in Figures 9 and 11 exemplify the self-consistent constitutive relation that governs the breakdown process during the nucleation.

4.1.2. Smooth fault. To demonstrate the effect of the fault surface roughness on shear rupture nucleation, comparisons are made between shear rupture that nucleated on a rough fault and that which is nucleated on a smooth fault. Figure 12 shows plots of the shear load (output signal from force transducer VFT in Figure 3) and the relative displacement measured between both ends of the sample blocks A and

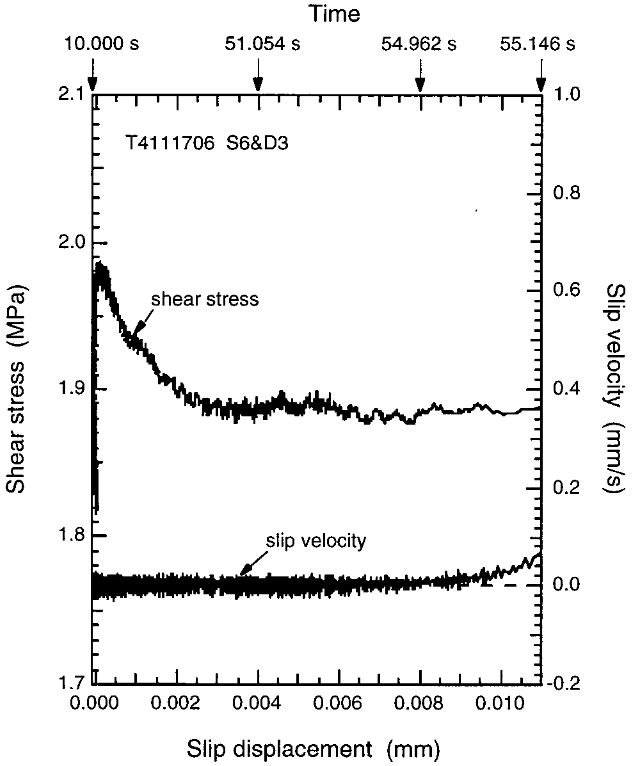

Figure 11. A plot of the shear stress measured at S6 against the slip displacement at the same position (D3) during the nucleation for the failure event (T4111706) shown in Figure 10 (rough fault). The slip velocity is also plotted against the slip displacement, and the time axis is added to facilitate comparison with Figure 10.

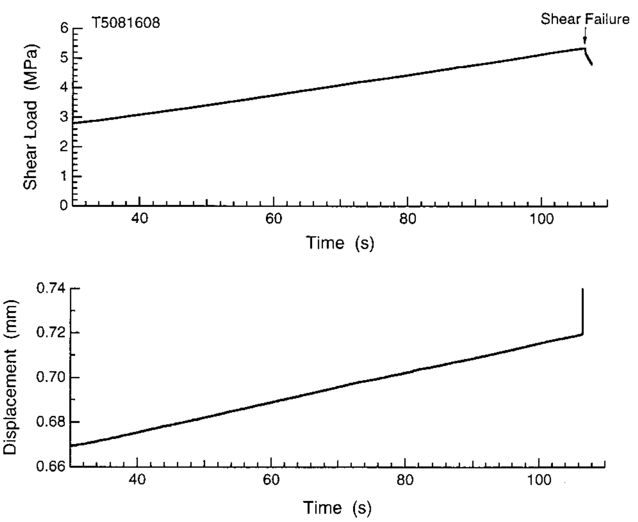

Figure 12. An example (event T5081608) of time records of remotely applied shear load and the relative displacement between both ends of the sample blocks A and B for a slip failure event on the smooth fault.

B along the fault, against time for a typical example of slip failure that occurred on the smooth fault. The origin of time *t* has been set such that $t = 0$ when the shear load began to increase for this slip failure. In stick-slip experiments, residual friction remains on the fault after the previous slip failure, and hence the magnitude of shear load is not nought at the beginning ($t = 0$) of the next stick-slip cycle, except for the first cycle of stick slip. The residual friction averaged over the entire fault was of 2.4 MPa at $t = 0$ for the slip failure shown in Figure 12. The shear load was elevated at a constant deformation rate of 6.6×10^{-4} mm/s under the remotely applied normal load of 6.2 MPa. It is not possible to discern from Figure 12 any strength degradation or slip acceleration phase as an indicator of the nucleation prior to overall failure along the fault.

Figure 13 shows a plot of the series of observed local shear stress data against time and distance along the fault for the failure event shown in Figure 12. Figure 13 shows how nonuniform the distribution of local shear stresses induced and accumulated during shear load application are on this smooth fault. It is suggested from Figure 13 that this particular fault can be characterized by the following two distinctive features: (1) inhomogeneous distribution of shear stresses on the fault that contains a predominant wavelength component of 5 cm, and (2) the minimum shear stress that is attained at one end of the fault length. These features obviously differs from those of the rough fault. Since the normal and shear loads were remotely applied uniformly in the experiments, we postulate that the observed distinctive features on this smooth fault arose from topographic irregularity of the fault surfaces produced during the preparation of the surface roughness. Figure 13 also indicates that the pattern of nonuniform distribution of local shear stresses initially induced on the fault was well preserved during the entire process of shear load application up to the overall failure.

The shear strength and stress nonuniformity on the fault may be more clearly seen in Figure 14. The data shown in Figure 14 are taken from the same data set shown in Figure 13. The top thick folded line in Figure 14 represents the distribution of the peak shear strength on the fault, and the bottom thick line represents the distribution of residual friction on the fault after the previous stick-slip failure. A series of thin folded lines in Figure 14 shows levels of local shear stresses at 12

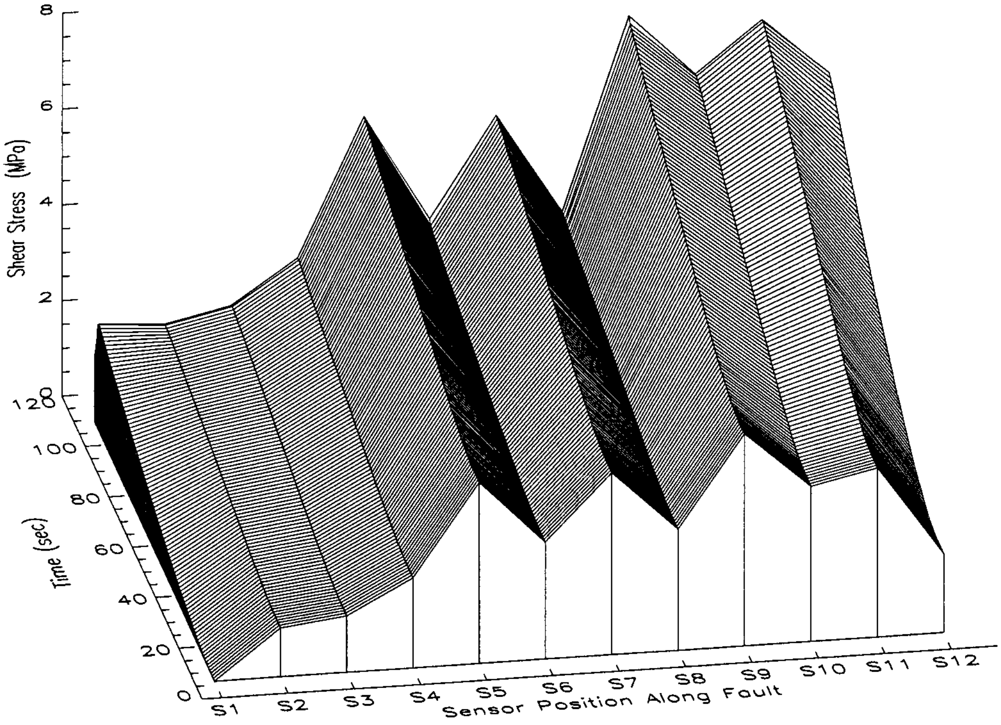

Figure 13. Time and spatial variations of original shear stresses recorded locally at 12 positions along the fault for the slip failure event shown in Figure 12 (smooth fault).

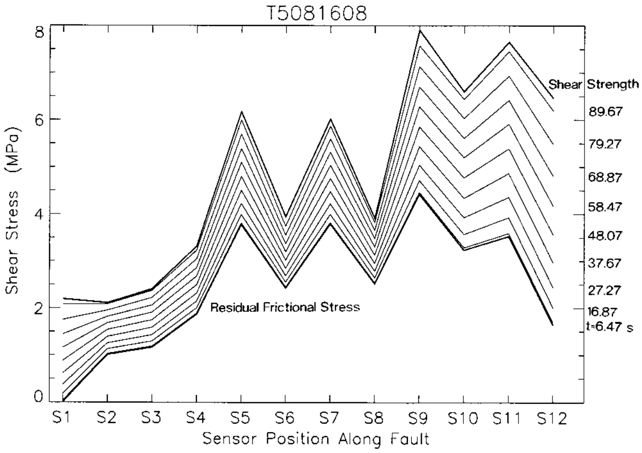

Figure 14. Nonuniform distributions of the fault strength, the residual friction stress, and variation of levels of local shear stresses along the fault with time for the slip failure event (T5081608) shown in Figures 12 and 13 (smooth fault). Local shear stress levels are plotted at 10.4-s intervals from $t = 6.47$ s after the onset of shear load application for this event.

positions (S1 through S12) along the fault during the process of shear load application, and these local stress levels are plotted at 10.4-s intervals from $t = 6.47$ s after the onset of shear load application. Figure 14 indicates that spatial distributions of both the fault strength (peak shear strength) τ_p and the residual friction τ_r on the fault are synclinally nonuniform and irregular with a predominant wavelength component of 5 cm, suggesting that there is a strong correlation between τ_p and τ_r. In fact, a strong positive correlation has been found between τ_p and τ_r for shear failure of intact rock under lithospheric conditions [*Ohnaka et al.*, 1997].

It has been found for slip failure on the rough fault that there is a higher rate of shear stress accumulation at the portion on the fault surface where the local strength is greater. This finding is corroborated by the present observation for slip failure on the smooth fault (Figure 14), and this fact may have an important implication because it means that the stress distribution on the fault is not independent of, but is closely related to, the distribution of fault strength throughout the entire process of stress accumulation.

In the experiment on slip failure shown in Figures 12 and 13, overall failure occurred around $t = 106.6$ s. However, it is not possible to identify from Figures 12 and 13 when and where slip failure began to nucleate. To make the time and location of the nucleation phase visible, local shear stresses measured in the vicinity of the fault are shown on an enlarged time axis scale in Figure 15. Figure 15 illustrates that the failure occurred over the entire fault around $t = 106.6$ s; however, no clear signal is evident to identify when and where rupture nucleation started.

An example of the series of shear stress records at 12 positions along the fault is shown in Figure 16 on enlarged scales of not only the time axis but also the stress axis to make the nucleation phase visible. This plot is for the same failure event shown in Figures 12–15, and the data are sampled every 10^4 point from the original data digitized at a sampling frequency of 1 MHz. Differential shear stress ($\tau_{d105.4871}$) in Figure 16 has been defined by

$$\tau_{d105.4871} = \tau - \tau_{t105.4871} \tag{7}$$

where τ represents a local shear stress measured at a position

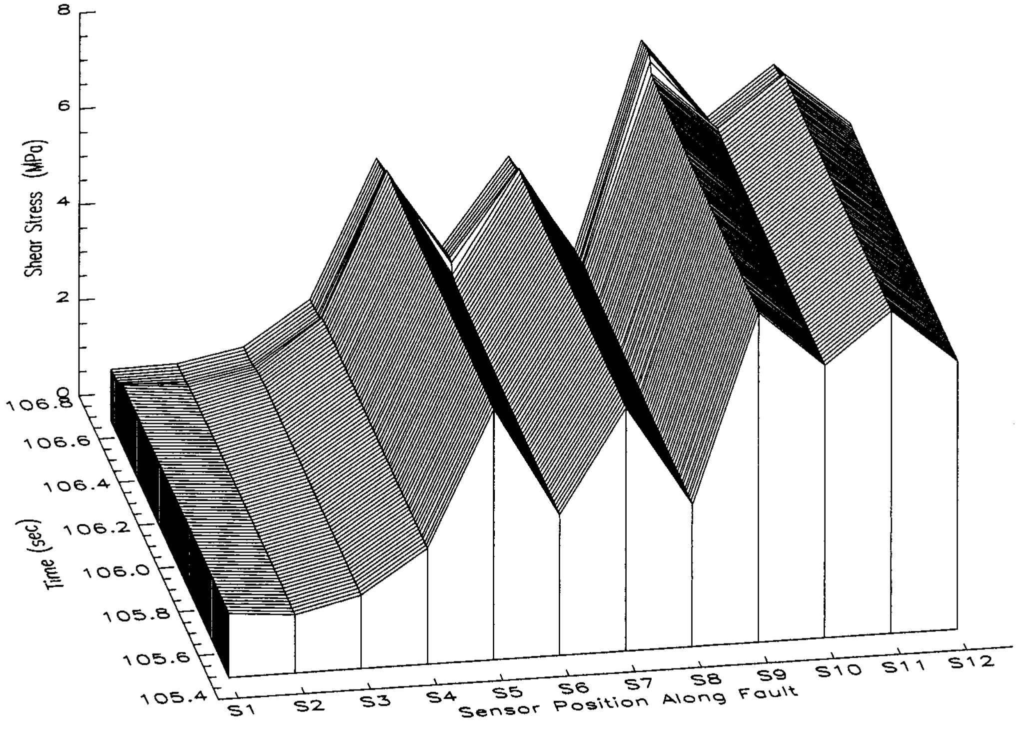

Figure 15. Time and spatial variations of original shear stresses recorded locally at 12 positions along the fault for the slip failure event shown in Figures 12–14: an enlarged detail on the time axis (smooth fault).

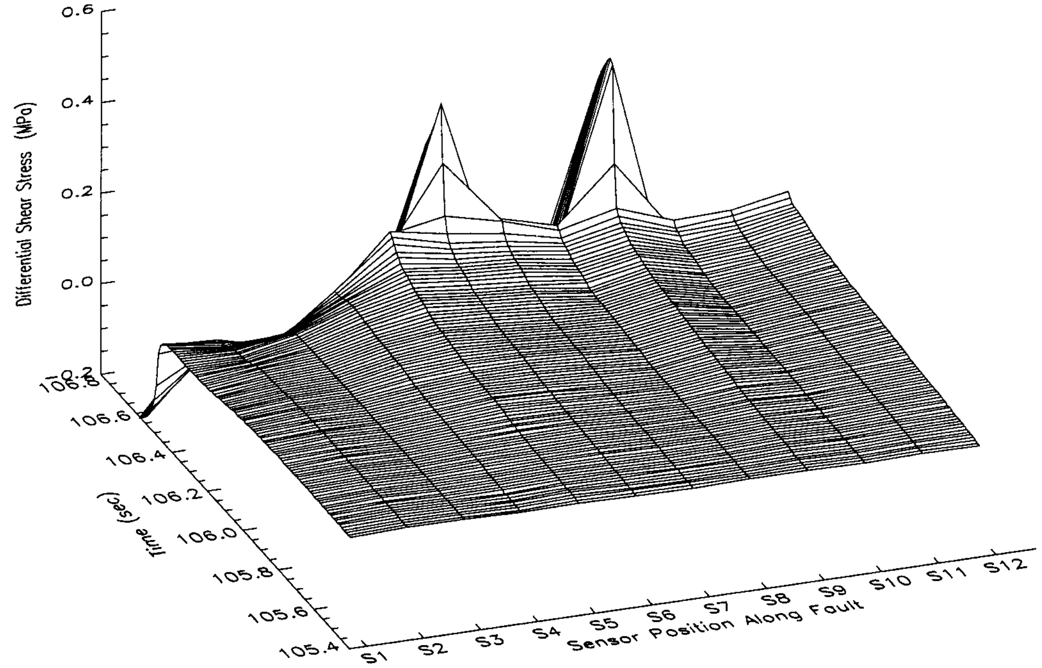

Figure 16. Time and spatial variations of differential shear stresses ($\tau_{\mathrm{d}105.4871}$) recorded locally at 12 positions along the fault during the nucleation for the slip failure event shown in Figures 12–15: an enlarged detail on both time and stress axes (smooth fault).

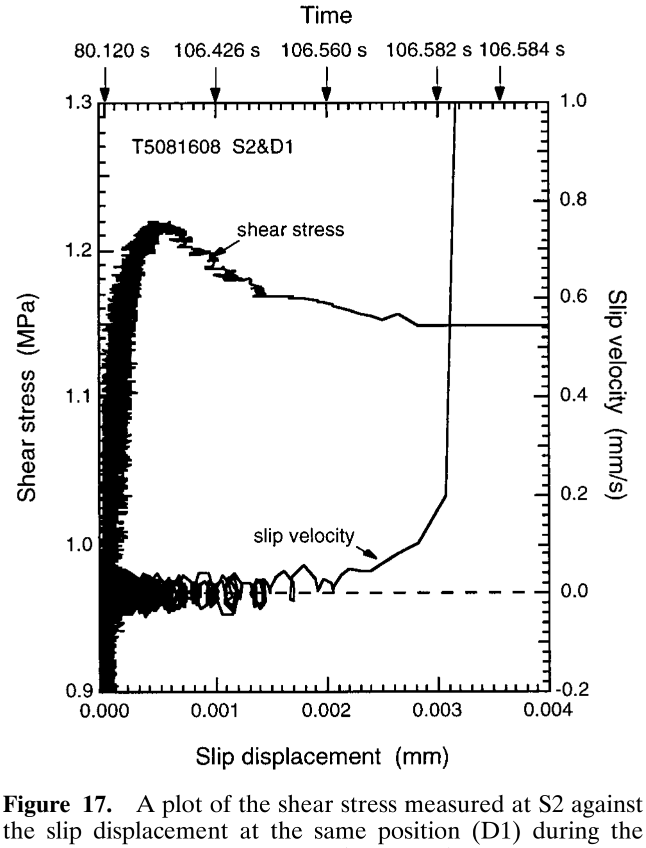

Figure 17. A plot of the shear stress measured at S2 against the slip displacement at the same position (D1) during the nucleation for the failure event (T5081608) shown in Figures 12–16. The slip velocity is also plotted against the slip displacement (smooth fault). The time axis is added to facilitate comparison with Figures 16, 23a, 23b, and 24a–24c.

along the fault and $\tau_{\mathrm{t}105.4871}$ represents the shear stress recorded at $t = 105.4871$ s at the same position.

We find from Figure 16 that local shear stresses at three positions S1, S2, and S3 along the fault began to degrade around $t = 106.6$ s, while the stresses at other positions slightly increased or hardly changed around $t = 106.6$ s. If viewed more carefully, we notice from Figure 16 that the shear stress began to degrade slightly at position S1 earlier than at any other positions along the fault, which will be seen more clearly in Figure 23a. This shows that the nucleation began to occur at one end of the fault and that the nucleation proceeded unidirectionally toward the other end of the fault. The observed slip-weakening relation in Figure 17 shows that shear rupture indeed occurred at a position of stress degradation. Comparison between Figures 16 and 17 may be facilitated by the time axis in Figure 17.

It has been found for the rough fault that the shear stress concentrates more at the location where the fault strength is locally higher; yet shear failure begins to nucleate around the location where the strength is the lowest. This is also corroborated by slip failure that occurred on the smooth fault. For instance, the rupture nucleation shown in Figure 16 began to occur around the location where the strength is the lowest (see Figure 14). One may argue that the nucleation that started at the lower edge of the fault could be ascribed to high stress concentration, which possibly occurs in the vicinity of the edge of sample block B. However, this argument is rejected because the stress cannot concentrate beyond the strength and because the strength is lowest near the lower edge of the fault. The condition at which the rupture begins to nucleate can be discussed more thoroughly in terms of the constitutive law for shear rupture in the framework of fracture mechanics. How-

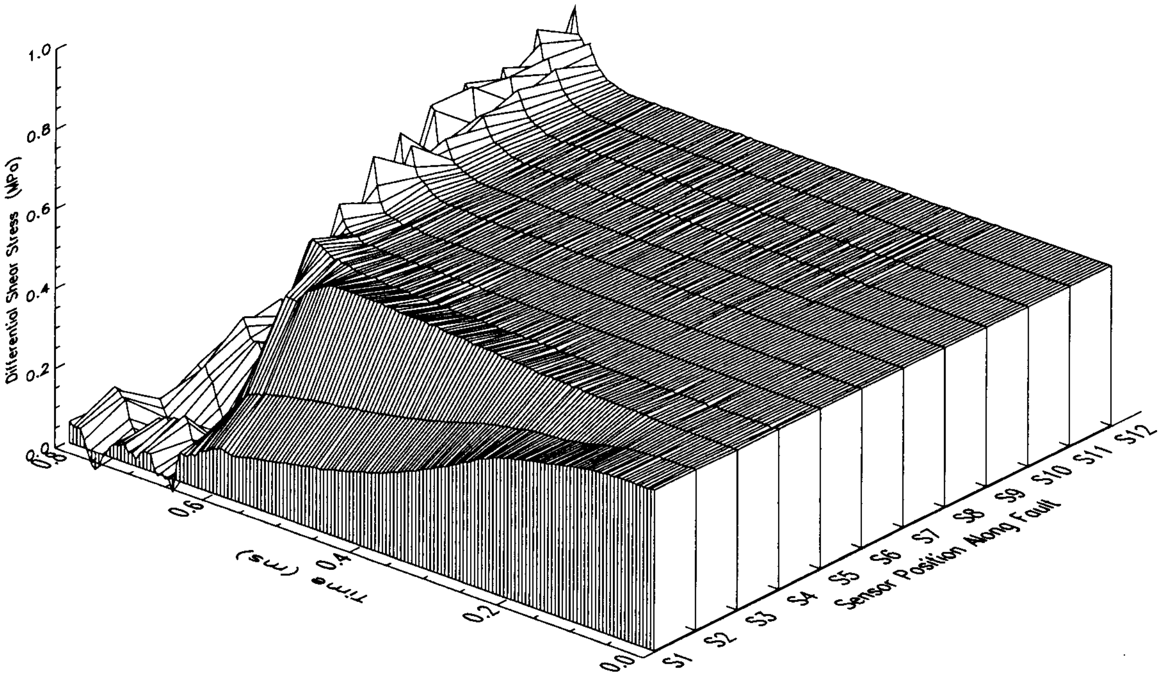

Figure 18. Time and spatial variations of differential shear stresses (τ_{d0}) recorded locally at 12 positions along the fault during the nucleation for a slip failure event on the extremely smooth fault.

ever, this is beyond the scope of the paper, and in-depth discussion about this will be made elsewhere.

If the nucleation that proceeded on the smooth fault (Figure 16) is compared with the nucleation on the rough fault (Figures 8 and 10), it is found that the nucleation zone size and its duration are much smaller for the event on the smooth fault than on the rough fault. These contrasting results suggest an implication of geometric irregularity of the fault surfaces for the nucleation.

Figures 15 and 16 indicate that the shear stress concentrated abruptly at two positions S6 and S9 when the front of shear rupture propagated dynamically on the fault. This suggests that the local strength was relatively higher than the local stress level at these two positions before the overall rupture and that local patches of the fault at these positions may have remained unruptured. This would occur if a local stress level did not attain the peak strength at the position when the rupture front passed through the position on the fault.

4.1.3. Extremely smooth fault. In the experiments on slip failure on the extremely smooth fault, metallic foil strain gauges with an active gauge length of 2 mm were used to measure local slip displacements along the fault, and amplified signals of local stress and slip displacement were sampled at a frequency of 1 MHz. On enlarged scales of both stress and time axes, Figure 18 shows a typical example of the series of shear stress records at 12 positions (S1 through S12) during the transition process from nucleation to dynamic rupture that took place on the extremely smooth fault. In this experiment the shear load was applied at a constant rate of 4.0×10^{-4} mm/s at the remotely applied normal load of 9.0 MPa. The origin of time t has been taken arbitrarily in Figure 18. Differential shear stress (τ_{d0}) in Figure 18 has been defined by

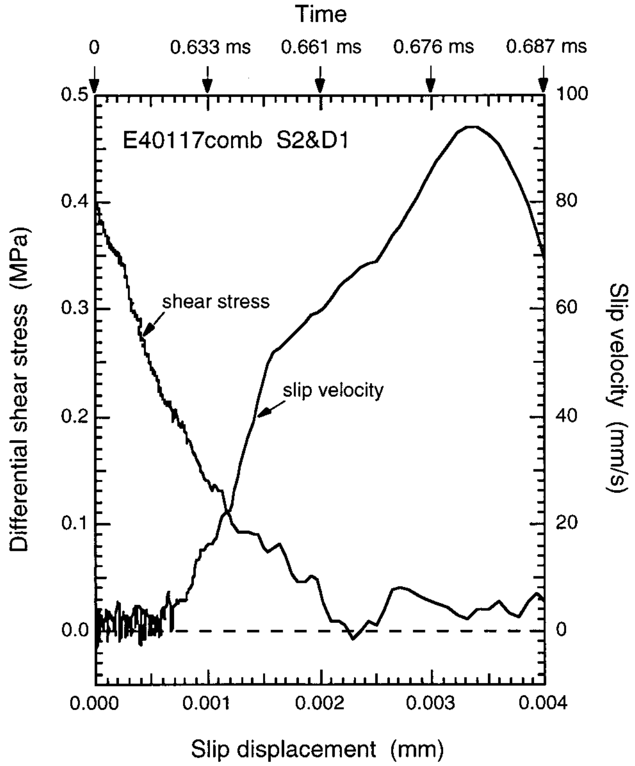

Figure 19. A plot of the shear stress measured at S2 against the slip displacement at the same position (D1) during the nucleation for the failure event (E40117comp) shown in Figure 18 (extremely smooth fault). The slip velocity is also plotted against the slip displacement. The time axis is added to facilitate comparison with Figure 18.

$$\tau_{d0} = \tau - \tau_{t0} + 0.4 \tag{8}$$

where τ represents a local shear stress measured at a time t at a position along the fault and τ_{t0} represents the shear stress recorded at $t = 0$ at the same position. In order to make the nucleation process more clearly visible in Figure 18, the entire data points have been shifted upward by 0.4 MPa on the stress axis in Figure 18, by adding 0.4 to the right-hand side of equation (8).

We find from Figure 18 that local shear stresses at two positions (S1 and S2) along the fault began to degrade around $t = 0.1$ ms, and that they continued to decrease thereafter, while the stresses at other positions remained constant until the stress pulse preceding dynamic rupture passed by. This leads to the conclusion that the nucleation began at one end of the fault and propagated unidirectionally to the other end of the fault. This can again be ascribed to the lowest strength at the lower edge of the fault.

It is obvious from Figures 8, 10, and 18 that the nucleation zone size and its duration on the extremely smooth fault are small compared with those on the rough fault. It will be shown later that the nucleation zone size and its duration on the extremely smooth fault are also smaller than those on the smooth fault. Figure 19 shows a slip-weakening relation observed at S2 (and D1) in the nucleation zone for the failure event shown in Figure 18. This demonstrates that slip failure actually occurred at a position of stress degradation.

4.1.4. Breakdown process: Transition from quasi-static to dynamic phase. We now turn our attention to how the breakdown (or slip weakening) process develops from quasi-static phase to dynamic phase in the nucleation zone and if the transition from quasi-static to dynamic phase is affected by geometric irregularity of fault surfaces. To discuss this on the basis of experimental data, the slip velocity is plotted against the slip displacement in Figures 9 and 11. The slip velocity in Figures 9 and 11 is the time derivative of the slip displacement smoothed by a moving average of three points. We find from Figure 9 that the slip velocity during the nucleation was substantially nought up to the slip amount of 8 μm, beyond which the slip velocity began to accelerate gradually. Yet the slip velocity remained very low (<0.12 mm/s) during the later phase of nucleation on the rough fault; for instance, the observed slip velocity was of 0.12 mm/s even at the slip displacement of 15 μm (Figure 9). Figure 11 also shows that the slip velocity during the nucleation on the rough fault was virtually nought up to the slip amount of 9 μm, after which it began to accelerate gradually. These features of slow process have been commonly observed during the nucleation on the rough fault. It can thus be concluded that the slip-weakening process during the nucleation on the rough fault was virtually stable and quasi-static.

In Figure 17 the slip velocity, which is the time derivative of the slip displacement smoothed by a moving average of five points, is also plotted against the slip displacement for a slip failure event on the smooth fault. We find from Figure 17 that the slip velocity during the nucleation on the smooth fault was virtually nought up to the slip amount of 2 μm. However, the slip velocity began to accelerate gradually beyond the slip amount of 2 μm, and eventually, it accelerated very rapidly at the slip displacement of 3 μm (Figure 17). This is contrasted with the nucleation that proceeded on the rough fault (Figures 9 and 11), in which the slip velocity remained very low (<0.1 mm/s) even beyond the slip amount of 10 μm (see Figures 9 and 11). These contrasting results suggest a significant implication of the fault surface irregularity (roughness) for the nucleation process.

The slip velocity during the nucleation on the extremely smooth fault is plotted against the slip displacement in Figure 19. The slip velocity in Figure 19 is the time derivative of the slip displacement smoothed by a moving average of nine points. One can see from Figure 19 that the slip velocity began to accelerate very rapidly at the slip displacement of 0.5–0.6 μm, which is far less than 2 μm. This is compared with the result obtained during the nucleation on the smooth fault, from which we can conclude that the slip-weakening process during the nucleation on the extremely smooth fault is less stable and more dynamic than the slip weakening during the nucleation on the smooth fault.

The above series of consistent results suggest that the critical slip displacement D_{sc}, which is defined here as the slip displacement below which the slip velocity is substantially nought during the nucleation, may scale with the characteristic length representing topographic irregularity of the fault surfaces. This will be checked here. If 200 μm is employed as the effective characteristic length λ_c for the rough fault (see section 2), we have that $D_{sc}/\lambda_c = 0.040$ for the data shown in Figure 9 and that $D_{sc}/\lambda_c = 0.045$ for the data in Figure 11. If 46 μm is employed as the effective characteristic length λ_c for the smooth fault, we have that $D_{sc}/\lambda_c = 0.043$ for the data in Figure 17. If 10 μm is employed as the effective characteristic length λ_c for the extremely smooth fault, we have that $D_{sc}/\lambda_c =$ 0.05–0.06 for the data in Figure 19. Note that 200, 46, and 10 μm each represent a characteristic length for the rough, smooth, and extremely smooth faults, respectively (section 2). The ratio D_{sc}/λ_c being constant (~0.05) for all these surfaces indicates that the critical slip displacement D_{sc} scales with the characteristic length representing the fault surface irregularity. Why D_{sc} has a value of $0.05\lambda_c$ is left for a future study. The effect of geometric irregularity of the fault surfaces on the nucleation will be further clarified and discussed in quantitative terms in sections 4.2 and 5.

4.2. Two Phases of Nucleation

4.2.1. Rough fault. Figures 20a and 20b show an example of shear stress versus time records at 12 positions (S1 through S12) along the fault and slip displacement versus time records at five positions (D1 through D5) for a slip failure nucleation on the rough fault. This particular event has been exemplified as a representative failure nucleation on the rough fault in the previous section (Figures 5–9). Arrows in Figure 20a indicate the time when slip failure began to occur locally at individual positions along the fault, which is defined here as the time when local stress record at the position has its peak value. It is clearly seen from Figure 20a how shear rupture nucleated and extended bidirectionally along the fault. Figure 20b shows that local slips at positions D1, D2, and D3 proceeded slowly prior to the imminent, overall dynamic slip failure. These local slow preslips correspond to local shear stress degradation at the same positions during the nucleation.

We can confirm from Figures 20a and 20b that the rupture nucleation proceeded under the condition that both ends of sample blocks A and B were servo-controlled to move at a constant rate (6.7×10^{-4} mm/s) in the fault length direction, a record of which is shown as overall displacement in the bottom frame of Figure 20b. This record shows that overall slip movement between both ends of the fault was well controlled

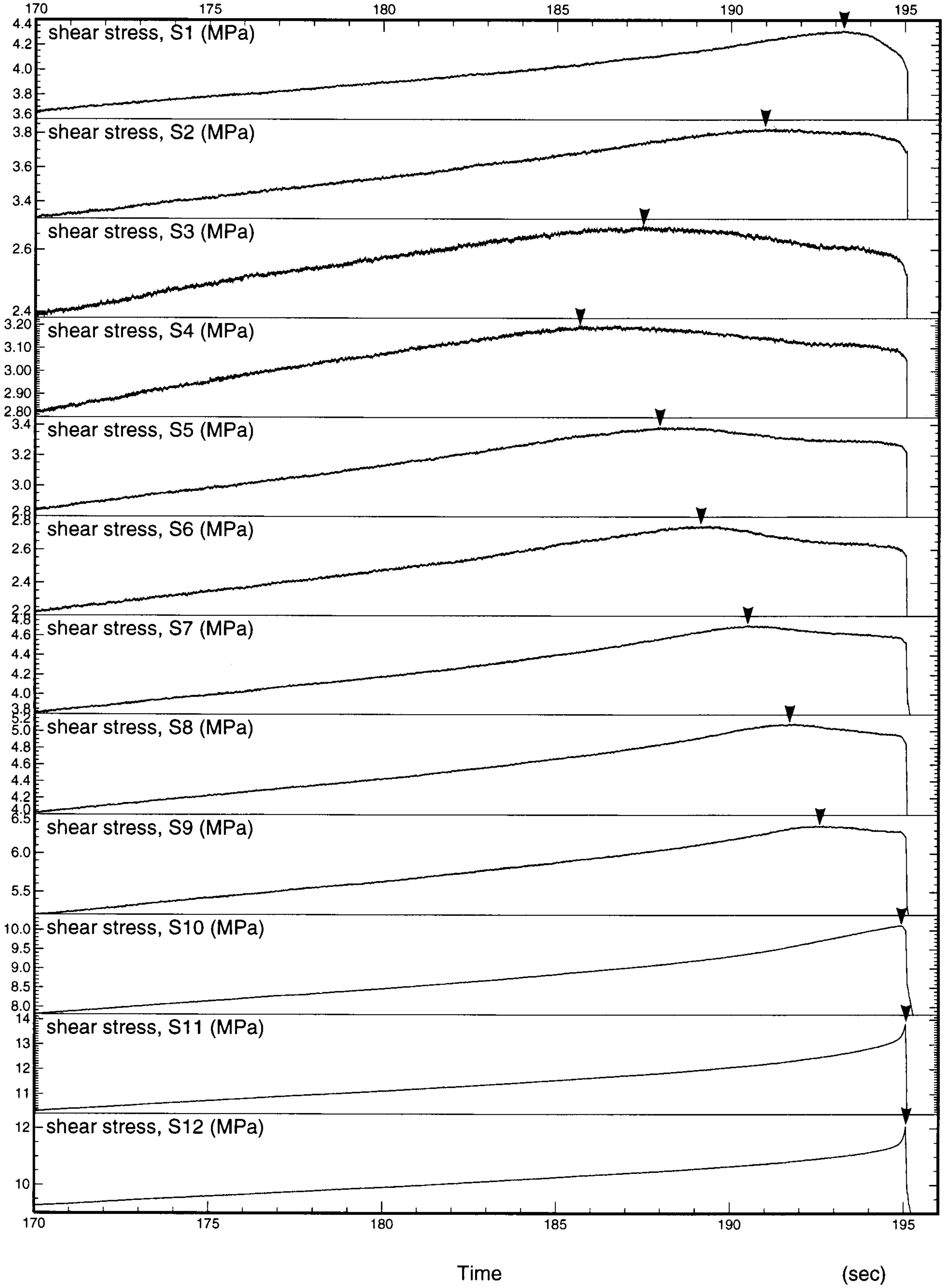

Figure 20a. An example (event T4111805) of local shear stress versus time records at 12 positions along the fault for a slip failure event on the rough fault. Arrows denote the time when slip failure began to occur locally.

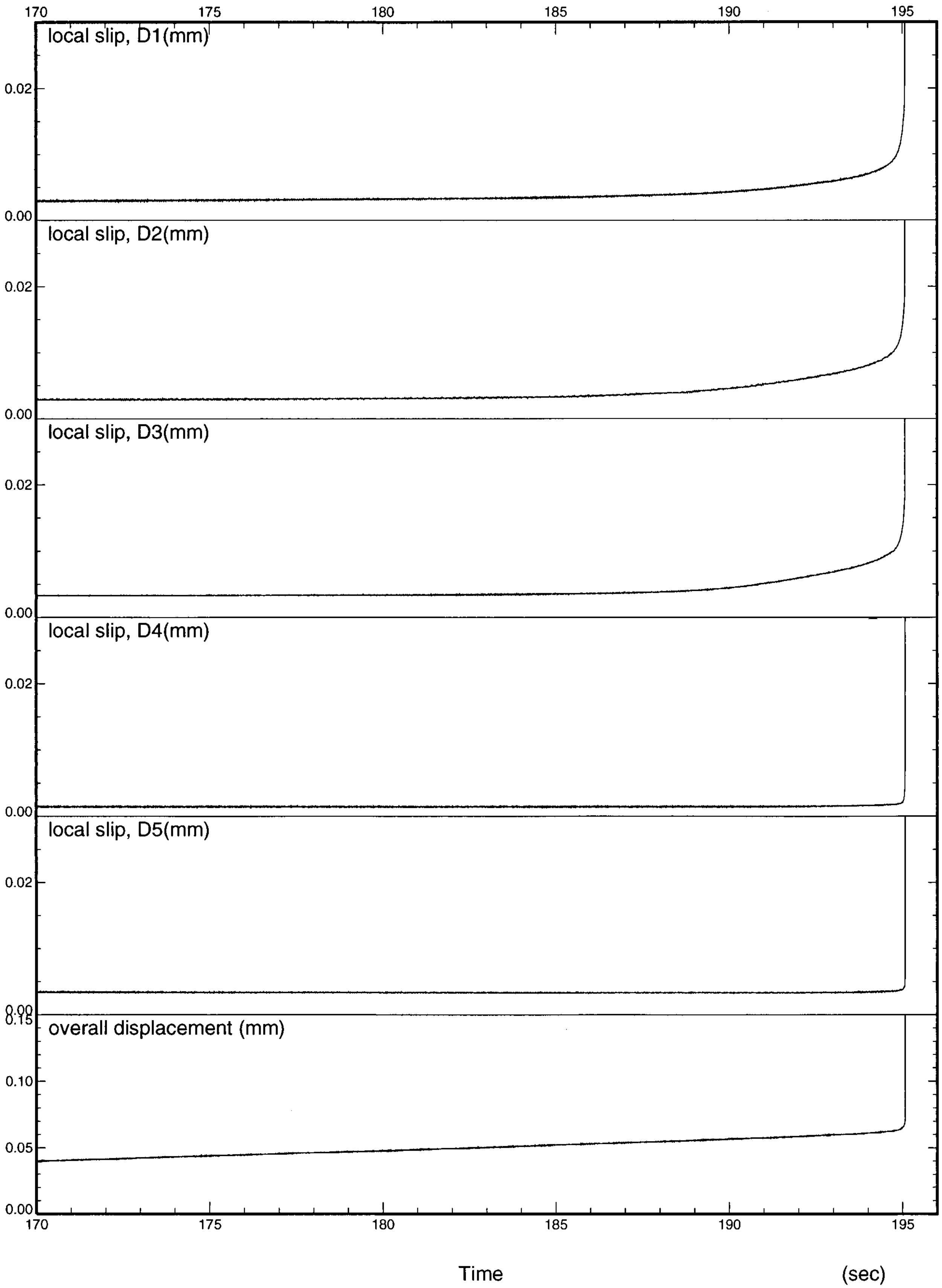

Figure 20b. Local slip displacement versus time records at five positions, D1 to D5, along the fault, and a time record of the relative displacement between both ends of sample blocks A and B (bottom frame), for the event shown in Figure 20a (rough fault).

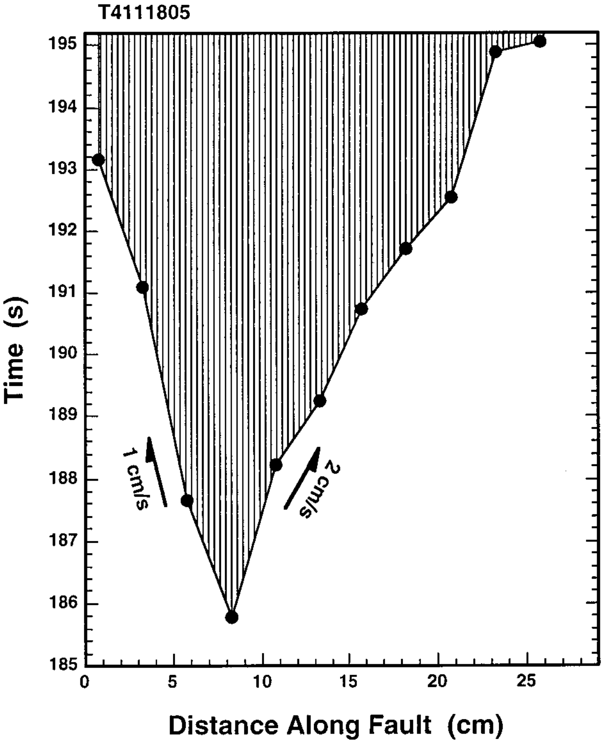

Figure 21. Space-time view of the nucleation zone on the rough fault for the event (T4111805) shown in Figure 20. The hatched portion indicates the zone in which the slip weakening is proceeding with time (see Figure 9).

up to the time $t = 195$ s, when overall dynamic slip failure occurred.

In Figure 21, the time when the rupture began to occur locally at individual positions S1 to S12 is plotted against the distance along the fault for the event shown in Figure 20. The hatched portion in Figure 21 indicates the zone in which the breakdown (or slip weakening) is proceeding with time. Figure 21 clearly shows how progressively the nucleation grew with time and allows one to evaluate the local rupture growth rate (or rupture velocity) V from the slope of a segment connecting the neighboring two points.

Figure 22 shows a plot of the logarithm of the rupture growth rate V against the logarithm of the rupture growth length L for several failure events which occurred on the rough fault. The experiments under the present conditions (the normal stress being of 6.2 MPa and the deformation rate being of 6.7×10^{-4} mm/s) led to the common observations that the rupture nucleation on the rough fault proceeded with distance at slow, steady velocities, with the fluctuation in the range 1–10 cm/s (Figure 22), suggesting that the nucleation on the rough fault grew stably over the entire fault length of 29 cm.

Accelerating phase of nucleation and the subsequent phase of high-speed rupture at a velocity close to sonic velocities were not observed for any event on the rough fault, despite the fact that these phases were clearly observed for events on smoother faults. We postulate that this was because the fault size of 29 cm was too short to observe the accelerating phase and the subsequent phase of high-speed rupture on the rough fault. Overall rupture was induced along the entire fault, immediately after the rupture front reached either end of the fault. We postulate that this is because such overall rupture was triggered by the break out of either end of the fault. If the length of this particular rough fault had been sufficiently large, such overall rupture would not have occurred at the rupture growth length of 29 cm or less.

4.2.2. Smooth fault. Figures 23a and 23b show an example of the series of shear stress versus time records and slip displacement versus time records along the fault for slip failure nucleation on the smooth fault. This event has been presented as a representative example for the nucleation on the smooth fault in the previous section (Figures 12–17). Again, from Figure 23a one can identify the time when slip failure began to occur locally at positions S1 to S12 on the fault. Arrows in Figure 23a indicate the time when slip failure began to occur locally at individual positions along the fault. We can confirm from Figure 23a that shear rupture indeed began to nucleate at one end of the fault and that it extended unidirectionally toward the other end of the fault. Figure 23b shows that slow slip began to proceed locally at position D1, prior to the imminent overall slip failure. This local, slow slip corresponds to shear stress degradation at the same position in the nucleation zone. In contrast, however, slip occurred abruptly without any slow preslip in the zone of dynamic rupture propagation (positions D3, D4, and D5 in Figure 23b). Note, in particular, from Figure 23b (and Figure 20b) that the observation of abrupt slip without any slow slip at one position near the fault never leads to the conclusion that there is no nucleation process of unstable, dynamic high-speed rupture. Figures 23a and 23b exemplify that in order to detect the nucleation that proceeds in a localized zone with time, it is critical to monitor spatial changes

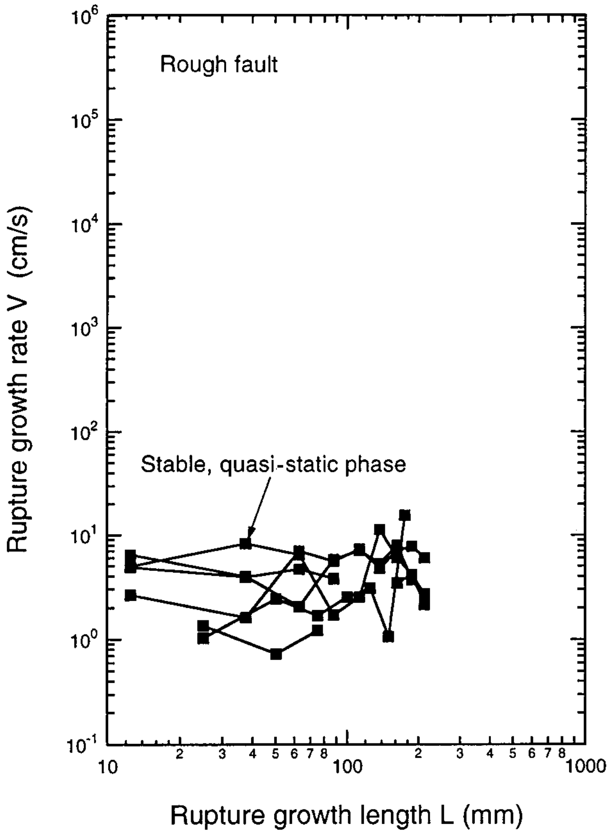

Figure 22. Plots of the logarithm of the rupture growth rate V against the logarithm of the rupture growth length L during the nucleation for events on the rough fault.

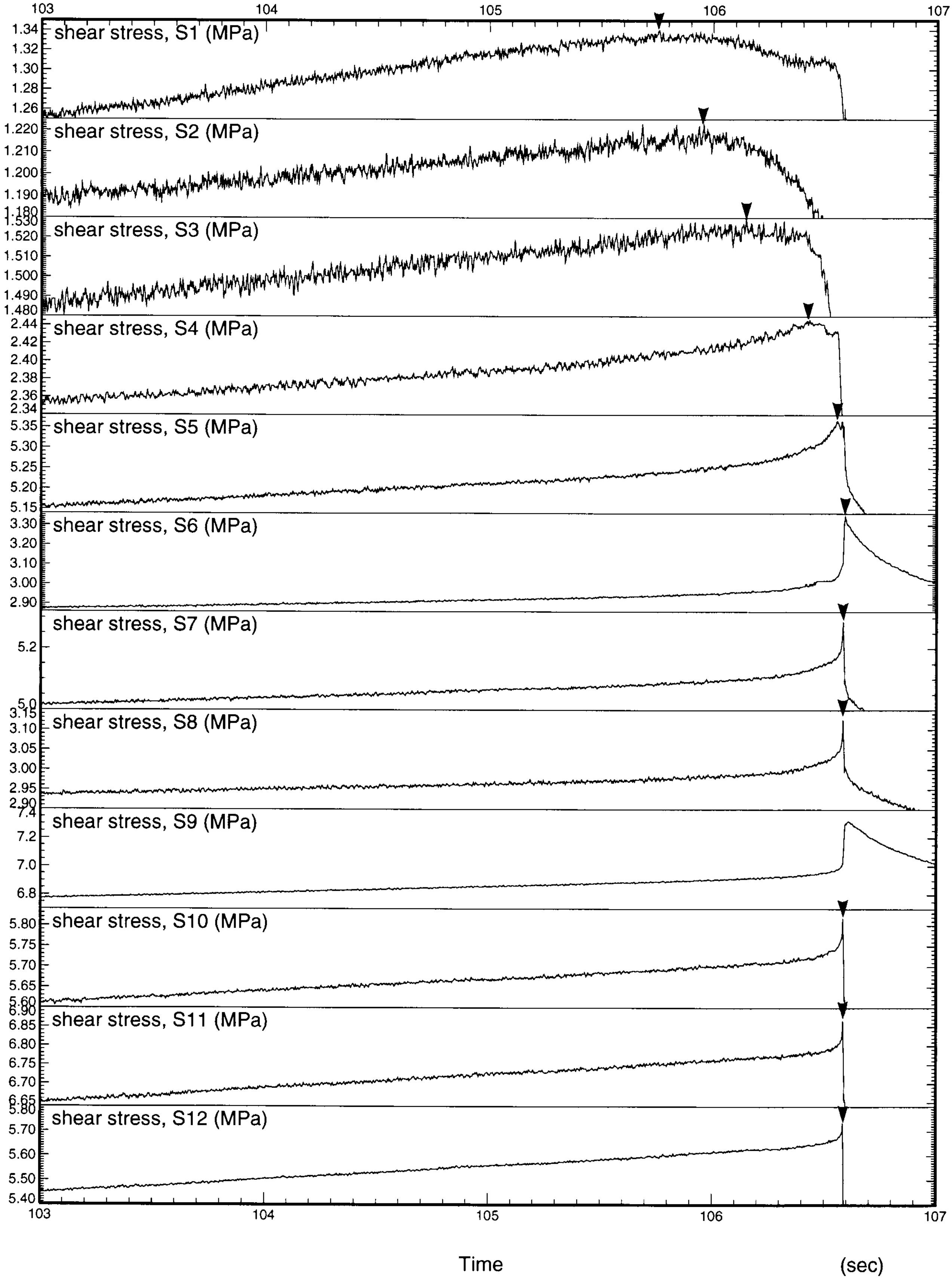

Figure 23a. An example (event T5081608) of local shear stress versus time records at 12 positions along the fault for a slip failure event on the smooth fault. Arrows denote the time when slip failure began to occur locally.

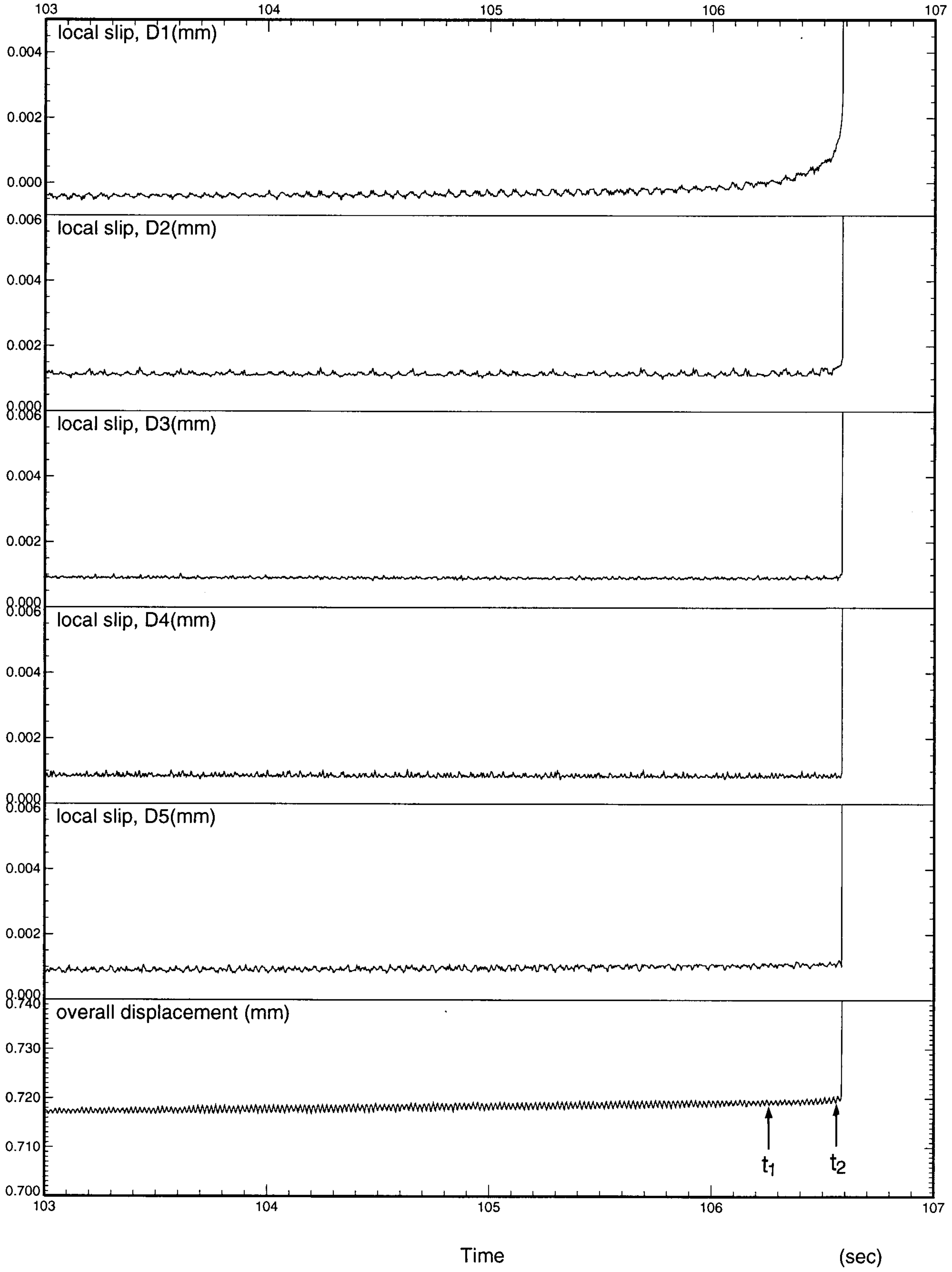

Figure 23b. Local slip displacement versus time records at five positions, D1 to D5, along the fault and a time record of the relative displacement between both ends of sample blocks A and B (bottom frame) for the event shown in Figure 23a (smooth fault). During the time span between t_1 (= 106.255 s) and t_2 (= 106.560465 s), the rupture locally extended unstably at accelerating speeds (see Figure 25).

of a series of local shear stresses and slip displacements measured in the vicinity of the fault.

Figure 24a shows a plot of the time when the rupture began to occur locally at positions S1 to S12 against the distance along the fault for the event shown in Figure 23, and the time axis of Figure 24a is enlarged in Figures 24b and 24c to make the nucleation process at later stages visible. The hatched portion in Figures 24a–24c indicates the zone in which the breakdown (or slip weakening) is proceeding with time. The series of Figures 24a–24c show how progressively the nucleation proceeded with time; that is, the nucleation at first grew slowly at an approximately constant velocity of 10 cm/s (Figure 24a), and shortly it began to extend with accelerating speeds to the other end of the fault (Figures 24b and 24c). This is more clearly seen in Figure 25, which shows log-log plots of the rupture growth rate V against the rupture growth length L for three independent failure events on the smooth fault. The rupture growth rate V in Figure 25 has been evaluated from the slope of a segment connecting the neighboring two points in Figures 24a, 24b, and 24c.

Figure 25 conclusively demonstrates that the nucleation process consists of two phases: phase I, an initial, quasi-static phase, which leads to phase II, the accelerating phase at a later stage. In phase I the rupture grows at a steady velocity, whereas in phase II the rupture grows very rapidly with accelerating speeds. In these experiments, both ends of the sample blocks were servo-controlled to move at a constant rate (6.6×10^{-4} mm/s) in the fault length direction, whose record is shown as overall displacement in the bottom frame of Figure 23b. This record clearly shows that overall slip movement between both ends of the fault was well controlled up to the time $t = 106.8$ s, when overall dynamic slip failure occurred. However, a local slip movement at any position within the fault zone is not

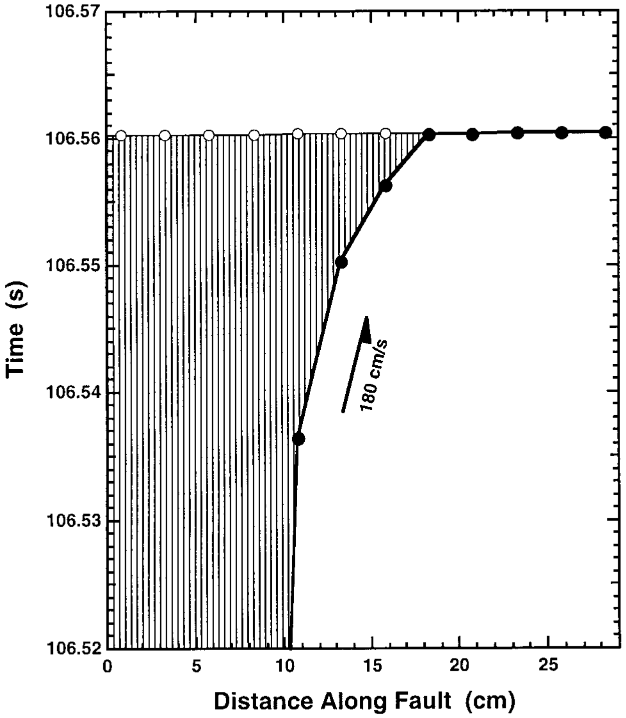

Figure 24b. Space-time view of the nucleation zone on the smooth fault for the event (T5081608) shown in Figure 23 on an enlarged time axis. The hatched portion indicates the zone in which the slip weakening is proceeding with time.

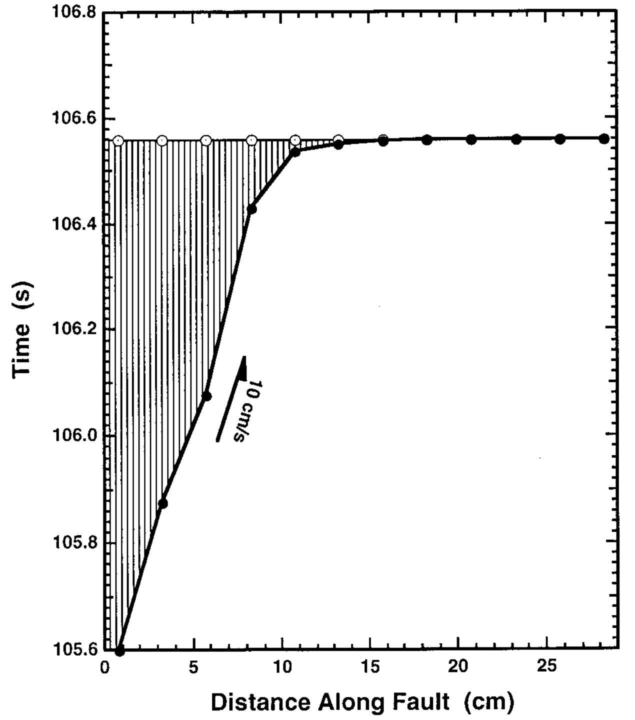

Figure 24a. Space-time view of the nucleation zone on the smooth fault for the event (T5081608) shown in Figure 23. The hatched portion indicates the zone in which the slip weakening is proceeding with time.

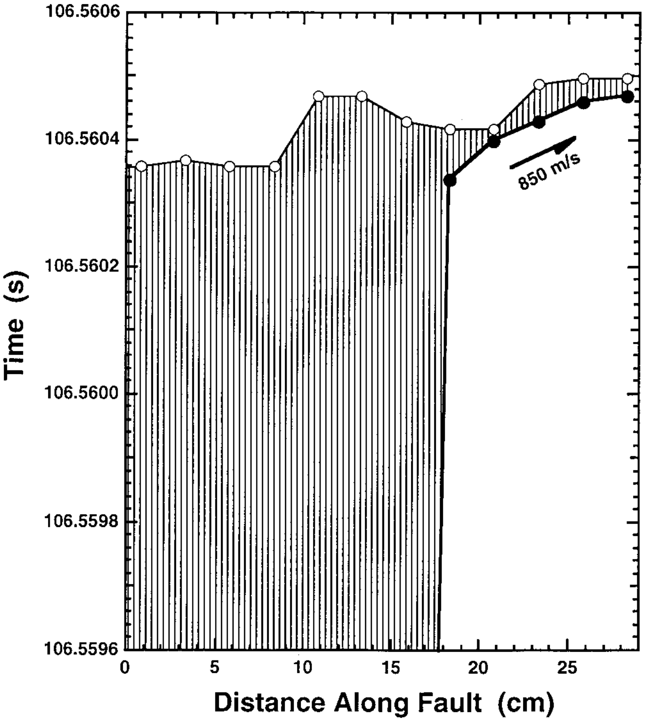

Figure 24c. Space-time view of the nucleation zone on the smooth fault for the event (T5081608) shown in Figure 23 on a more enlarged time axis. The hatched portion indicates the zone in which the slip weakening is proceeding with time.

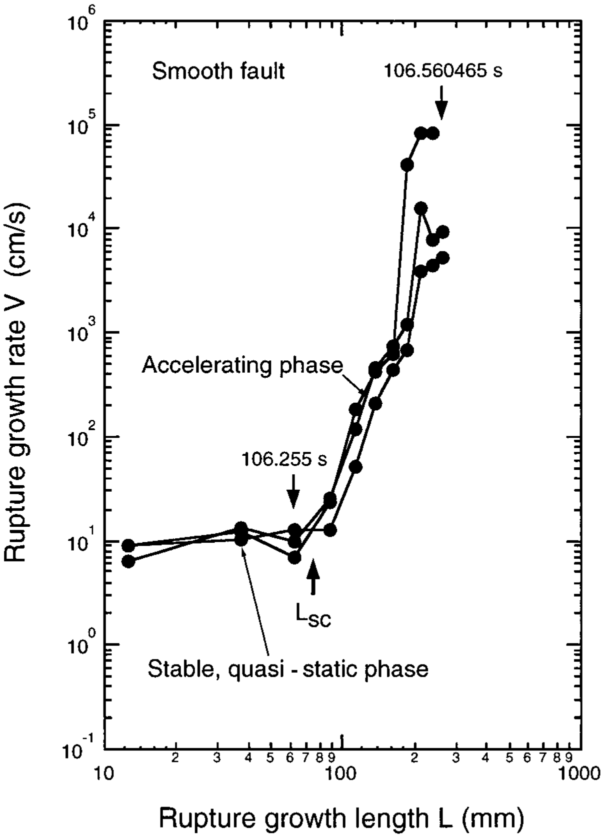

Figure 25. Plots of the logarithm of the rupture growth rate V against the logarithm of the rupture growth length L during the nucleation for events on the smooth fault. L_{sc} denotes the critical length beyond which the rupture grows at accelerating speeds, and the times $t_1 = 106.255$ s and $t_2 = 106.560465$ s are included to facilitate comparison with Figures 23 and 24.

controlled, and therefore the rupture can propagate unstably at accelerating speeds in a localized zone on the fault, even when both ends of the fault are moved at a controlled, slow steady speed of 6.6×10^{-4} mm/s. This is possible when the elastic strain energy stored near the fault in the sample blocks is released and when the released energy exceeds the energy consumed for further growth of the rupture (fracture energy). This is attained after the rupture grows beyond a critical length L_{sc} (Figure 25). In fact, it is confirmed from comparison between Figures 23b and 25 that the fault movement was indeed well controlled over the time span between $t_1 = 106.255000$ s and $t_2 = 106.560465$ s during which the rupture developed at accelerating speeds. Phase II is thus essentially an unstable process.

The result presented in Figure 25 is very significant because this is the first successful observation of the transition process from the phase of stable, slow growth of rupture to the subsequent accelerating phase of rupture growth for single events. The experiments under the present conditions (the normal stress being of 6.2 MPa and the deformation rate being of 6.6×10^{-4} mm/s) led to common observations of these two phases on the smooth fault, with good reproducibility.

However, the terminal phase of fast rupture at a speed close to the shear wave velocity was not observed for events on the smooth fault, although the terminal phase was commonly observed for events on the extremely smooth fault that will be discussed in section 4.2.3. These results suggest that the entire process from the quasi-static phase of nucleation to the accelerating phase and to the terminal phase of high-speed rupture can be observed for a single event only if the fault has sufficient length. We postulate that the fault length of 29 cm was too short to observe the terminal phase of high-speed rupture on the smooth fault.

4.2.3. Extremely smooth fault. Figure 26 shows a plot of the time when the rupture began to occur locally at positions S1 to S12 against the distance along the fault for the event shown in Figure 18. The hatched portion in Figure 26 indicates the zone in which the breakdown (or slip weakening) is proceeding with time. In Figure 27 the rupture growth rate V is plotted against the rupture growth length L for four events that developed on the extremely smooth fault. Figures 26 and 27 show how rapidly the rupture accelerates up to the terminal phase of its high-speed propagation on the extremely smooth fault. The rupture eventually propagated at a steady speed close to the shear wave velocity (2.9 km/s) on this particular fault. This is contrasted with the phase of slow rupture growth on the rough fault. The rupture growth rate V evaluated from the slope of a segment connecting the neighboring two points in Figure 26 gave the lowest value of 50 m/s in the nucleation zone (Figure 26), which is much higher than initial velocities (of the order of 1–10 cm/s) observed during the nucleation on the rough and smooth faults. No phase of stable, slow growth of rupture (phase I) was observed for slip failure on the extremely smooth fault. We postulate that this is because phase I did not develop fully to the measurable extent on the extremely smooth fault and because the size of phase I which might have appeared on the extremely smooth fault was too small to be measured with strain gauge sensors mounted at every 25 mm space interval along the fault. If the space interval

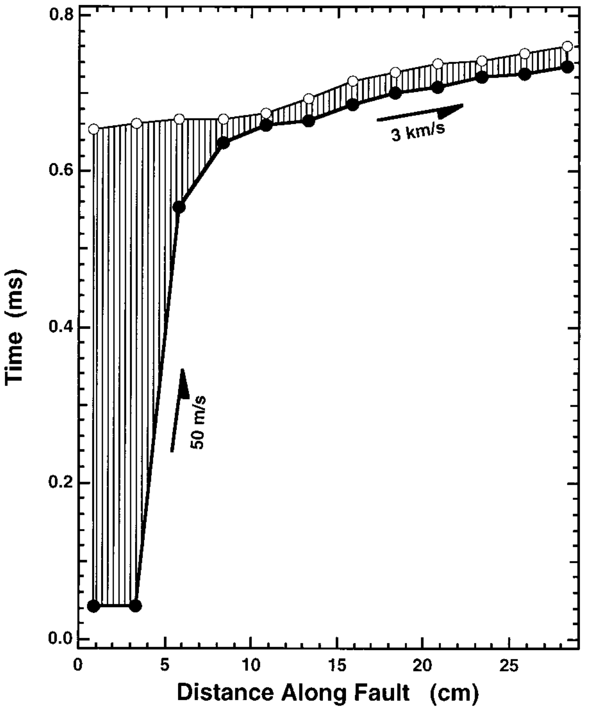

Figure 26. Space-time view of the nucleation zone for a slip failure event (E40117comb) on the extremely smooth fault. The hatched portion indicates the zone in which the slip weakening is proceeding with time.

between the neighboring two sensors had been much shorter than 25 mm, it might have been observed even on the extremely smooth fault.

The present series of high-resolution experiments on propagating shear rupture on faults with different surface roughnesses led to the conclusive results that the nucleation process consists of the two phases: an initial, quasi-static phase (phase I), and the subsequent accelerating phase (phase II), and that the temporal and spatial characteristics of these phases are scaled by geometric irregularity of the rupturing surfaces (see Figures 22, 25, and 27). One may argue, however, that the results presented here are too incomplete and inconsistent to provide a unified and consistent comprehension for the entire process from the quasi-static phase of nucleation to the terminal phase of fast-speed rupture propagation. To have a unified and consistent comprehension for this, we need an appropriate scaling parameter. This will be discussed in section 5.

5. Scaling of the Nucleation Zone Size and Its Duration: Comparison Between Experiment and Theoretical Analysis

5.1. Nucleation Zone Size

How can a unified comprehension and consistent interpretation be provided for the experimental results presented in the previous section? It has been demonstrated that a change in the breakdown process from a quasi-static phase to the subsequent dynamic phase on faults with different surface roughnesses can be explained consistently if the effective characteristic length λ_c is assumed to be 200 μm for the rough fault, 46 μm for the smooth fault, and 10 μm for the extremely smooth fault (section 4.1). One may thus expect that the rupture growth length L also scales with λ_c, given that the corner length λ_c defined in section 2 is a characteristic length scale representing the fault surface irregularity in the slip direction.

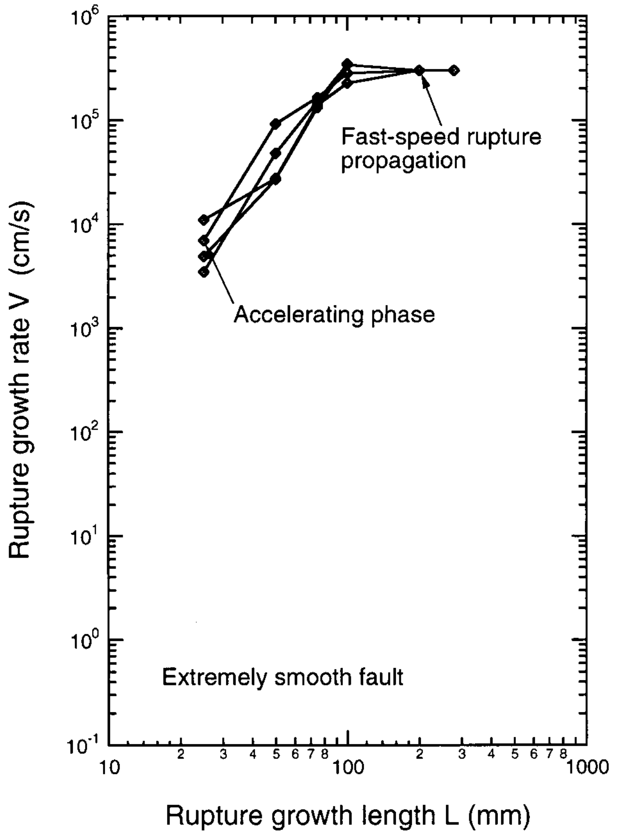

Figure 27. Plots of the logarithm of the rupture growth rate V against the logarithm of the rupture growth length L during the nucleation for events on the extremely smooth fault.

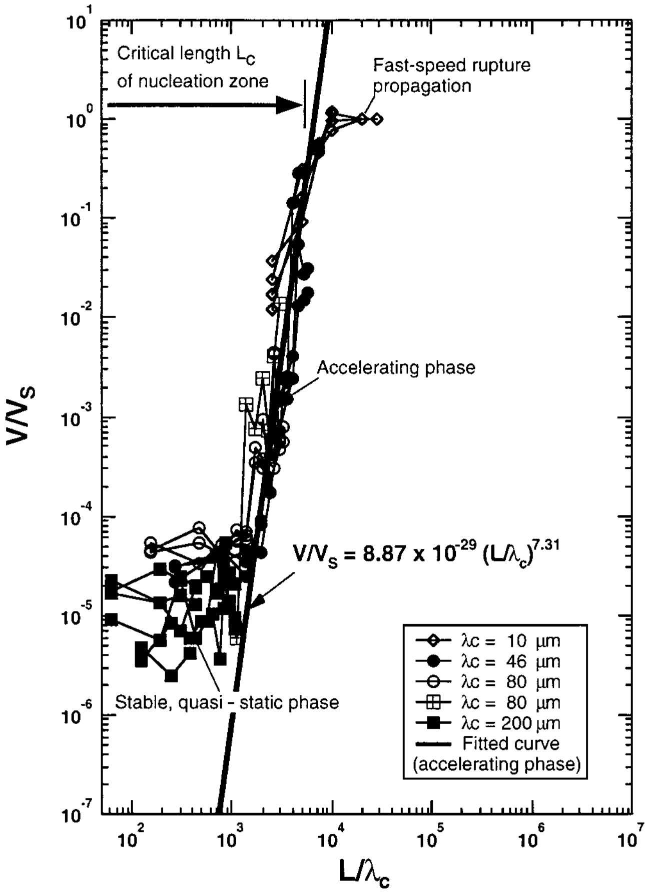

Figure 28. Log-log plots of the rupture growth rate V normalized to the shear wave velocity V_S against the rupture growth length L normalized to λ_c during the nucleation for events on the faults with different surface roughnesses.

With this expectation in mind, the rupture growth rate V normalized to the shear wave velocity V_s is plotted against L normalized to λ_c for the same data shown in Figures 22, 25, and 27 and for additional data in Figure 28. We find from Figure 28 that L indeed scales well with λ_c and that a unified comprehension can be provided for the entire data set on the rupture nucleation on faults with different surface irregularities. It is also found from Figure 28 that the entire data points in the accelerating phase fall around a single straight line on the log-log plot, showing that the accelerating phase obeys a power law of the form

$$\frac{V}{V_S} = \alpha\left(\frac{L}{\lambda_c}\right)^n \tag{9}$$

where α and n are numerical constants. The present data set in the accelerating phase gives $\alpha = 8.87 \times 10^{-29}$ and $n = 7.31$.

One may claim that the power law (9) empirically obtained above is only an artifact of the linear fit on the log-log plot, and that an exponential type of behavior is more physically reasonable for a self-amplifying process. However, a functional form of exponential type is found to be more poorly fitted to the present data set. In addition, a power law of the form

$$V = V_0 K_1^n \exp\left(-\frac{H}{RT}\right) \tag{10}$$

has been proposed [*Charles*, 1958] to explain the relation between the subcritical growth rate V of mode I crack and the crack tip stress intensity factor K_1, observed for a large body of experimental data on many different classes of materials, including rocks and minerals [e.g., *Atkinson*, 1982, 1984; *Atkinson and Meredith*, 1987]. In equation (10), V_0 and n are constants, H is the activation enthalpy, R is the gas constant, and T is the absolute temperature. Since K_1 is expressed in terms of the remotely applied stress σ and the crack length L as $K_1 = m\sigma\sqrt{L}$ (m, a dimensionless modification factor) in the framework of linear fracture mechanics, we find from (10) that the relation between the subcritical crack velocity V and the crack growth length L obeys the power law. In spite of different modes of rupture (modes I and II), equations (9) and (10) show that there is a clear phase in which the rupture extends at accelerating speeds with the rupture length, prior to the terminal phase of high-speed rupture close to sonic velocities, and that this accelerating phase is commonly described by the power law. This suggests that the accelerating phase is governed by the common, underlying physics.

Kuwahara et al. [1986] reported that the rupture growth rate V in phase I depends on the applied loading rate. This implies that phase I is a stable process, which is consistent with the present results. However, phase II in which the rupture develops at accelerating speeds V no longer depends on the applied loading rate but increases rapidly with an increase in L according to the power law (9). This again necessarily leads to the conclusion that the accelerating phase is essentially an unstable process. Figure 28 indicates that an increase in V/V_S with L/λ_c begins to deviate from the power law (9) at $L_c/\lambda_c = 5.6 \times 10^3$, suggesting that the rupture velocity V converges to a terminal velocity.

The present result provides an important implication for predicting the onset of dynamic, high-speed rupture, because it shows that the run-up distance is short to attain the high-speed rupture on smooth fault surfaces and because a long run-up is required for reaching the same speed on rough, irregular fault surfaces.

We consider from a theoretical viewpoint how the nucleation zone size and its duration scale with λ_c. We assume a rupture nucleation model shown in Figure 29. It is assumed in this model that the rupture begins to propagate bidirectionally at a fast, constant speed V_c at the critical time t_c. The hatched portion in Figure 29 shows the zone in which the breakdown (or slip weakening) is proceeding with time. In this model, the critical size $2L_c$ (L_c, half length) of the nucleation zone is related to the breakdown zone size X_c in the terminal phase of dynamic, high-speed rupture as follows:

$$\begin{aligned} L &< X_c \qquad t < t_c \\ L_c &= X_c \qquad t = t_c \end{aligned} \tag{11}$$

In the zone of dynamic high-speed rupture, X_c is directly related to the critical slip displacement D_c by [*Ohnaka and Yamashita*, 1989]

$$\frac{D_c}{X_c} = k\,\frac{\Delta\tau_b}{\mu} \tag{12}$$

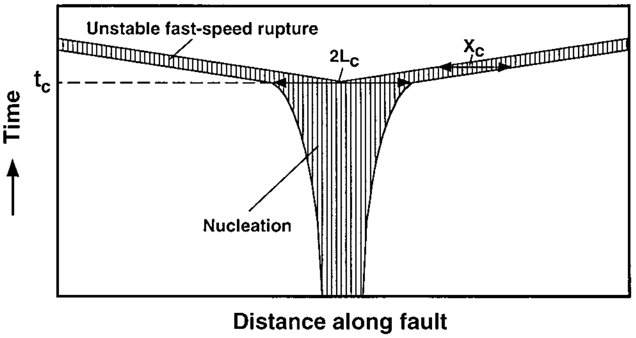

Figure 29. A rupture nucleation model. It is assumed in this model that the rupture begins to propagate bidirectionally at a fast, constant velocity V_c at the critical time t_c. X_c denotes the breakdown zone size, and $2L_c$ denotes the critical size of the nucleation zone.

where D_c has been defined as the slip displacement required for the local strength in the breakdown zone behind the rupture front to degrade to a residual friction stress level τ_r, $\Delta\tau_b$ represents the breakdown stress drop defined as the shear stress difference between the peak shear strength τ_p and τ_r, μ represents the rigidity, and k is a dimensionless quantity defined by [*Ohnaka and Yamashita*, 1989]

$$k = \frac{\Gamma}{\pi^2 C(V)\xi} \tag{13}$$

Here ξ is a numerical parameter, $C(V)$ is a known function of V, and Γ is a dimensionless quantity defined by [*Ohnaka and Yamashita*, 1989]

$$\Gamma = \int_0^1 \frac{\sigma(Y)}{\sqrt{Y}}\,dY \tag{14}$$

where $\sigma(Y)$ is the nondimensional shear strength at a nondimensional distance measured from the rupture front in the breakdown zone [see *Ohnaka and Yamashita*, 1989]. From (11) and (12) we have

$$L_c = \frac{1}{k}\,\frac{\mu}{\Delta\tau_b}\,D_c \tag{15}$$

Since k has a value of the order of unity [*Ohnaka*, 1996], equation (15) indicates that the critical size $2L_c$ of the nucleation zone is substantially determined by D_c and $\Delta\tau_b$.

It has been demonstrated in laboratory experiments that $\Delta\tau_b$ is related to D_c by [*Ohnaka*, 1996]

$$\frac{\Delta\tau_b}{\Delta\tau_{b0}} = \left(\frac{D_c}{\lambda_c}\right)^M \tag{16}$$

where $\Delta\tau_{b0}$ and M are constants. On the other hand, D_c is related to λ_c by [*Kuwahara et al.*, 1985; *Ohnaka*, 1992, 1996]

$$D_c = m(\sigma_n)\lambda_c \tag{17}$$

where $m(\sigma_n)$ is a numerical parameter which is an increasing function of σ_n. The relation (17) shows that the slip displacement D_c required for the slip-weakening zone behind the propagating rupture front to break down is directly related to the characteristic scale λ_c in the slip direction on the rupturing surfaces. The parameter $m(\sigma_n)$ may indicate the degree of coupling between the rupturing surfaces.

Combining (16) and (17) with (12) and (15) leads to [*Ohnaka*, 1996]

$$L_c = X_c = \frac{1}{k}\frac{\mu}{\Delta\tau_{b0}}\{m(\sigma_n)\}^{1-M}\lambda_c \tag{18}$$

Since k, μ, $\Delta\tau_{b0}$, and $\{m(\sigma_n)\}^{1-M}$ are size-scale-independent [*Ohnaka*, 1996], it follows that X_c and L_c each scale with λ_c [*Ohnaka*, 1996]. The experimental result (Figure 28) shows that the nucleation zone size (half length L) of $(5–6) \times 10^3\ \lambda_c$ is attained at $V/V_S = 0.3–0.6$. This experimental result agrees well with the theoretical estimate from equation (18). For instance, if it is assumed that the critical size of the nucleation zone is attained at a value in the V/V_S range 0.3–0.6 and that $\tau_i/\tau_p = 0.5–0.8$ [see *Ohnaka and Yamashita*, 1989], we have $L_c = (4.4–7.0) \times 10^3\ \lambda_c$ from equation (18) by considering that $\mu = 2 \times 10^4$ MPa for the granite sample used and assuming that $M = 1$ and $\Delta\tau_b = 3$ MPa [see *Ohnaka*, 1996, Figure 3]. We thus have the following approximate relation:

$$2L_c \simeq 10^4\lambda_c \tag{19}$$

for the critical size of shear rupture nucleation zone from both experiment and theoretical analysis. The relation agrees with the estimates in earlier preliminary studies [*Kuwahara et al.*, 1986; *Ohnaka*, 1996].

For actual earthquake faults the effective characteristic length λ_c can be inferred from relation (19), under the assumption that relation (19) is applicable to actual earthquake faults. The critical size of the nucleation zone has been estimated for a number of major earthquakes, showing that the critical size $2L_c$ for major earthquakes with $M = 7–8$ is of the order of 1–10 km [*Ohnaka*, 1993; *Ellsworth and Beroza*, 1995; *Beroza and Ellsworth*, 1996; *Shibazaki and Matsu'ura*, 1998]. For these major earthquakes, λ_c is estimated to be of the order of 10 cm to 1 m from relation (19). These values for λ_c are compatible with the critical slip displacement for major earthquakes [*Papageorgiou and Aki*, 1983; *Ide and Takeo*, 1997]. In fact, the critical slip displacement of the same order of slip amount has recently been estimated directly from inversion of near-field seismic waves for the 1995 Kobe earthquake ($M7.2$) [*Ide and Takeo*, 1997].

5.2. Duration

The time t_c needed for shear rupture to grow from a stage of the rupture growth length L in phase II to the critical length L_c beyond which the rupture propagates at a fast speed V_c close to sonic velocities is given by

$$t_c = \int_L^{L_c} \frac{dL}{V(L)} \tag{20}$$

We thus obtain from (9) and (20)

$$t_c = \frac{\lambda_c}{V_S} f\left(\frac{V}{V_S}, \frac{V_c}{V_S}\right) \tag{21}$$

where

$$f\left(\frac{V}{V_S}, \frac{V_c}{V_S}\right) = \frac{\alpha^{-1/n}}{n-1}\left(\frac{V_c}{\mathrm{V_S}}\right)^{(-\mathrm{n}+1)/\mathrm{n}}\left[\left(\frac{V/V_S}{V_c/V_S}\right)^{(-n+1)/n} - 1\right] \tag{22}$$

Since the rupture growth velocity V is a monotonically increasing function of the rupture growth length L in the accelerating phase, t_c in equation (21) has been expressed as an explicit function of the rupture velocity V in place of L. The theoretical relations (21) and (22) show that t_c scales with λ_c, because V_S and $f(V/V_S, V_c/V_S)$ are scale-independent. The time T_c $(= X_c/V_c)$ required for the slip-weakening zone behind the propagating rupture front to break down also scales with λ_c. These results show that the rougher the rupturing surfaces, the greater the timescales of shear rupture nucleation and the breakdown behind the rupture front are.

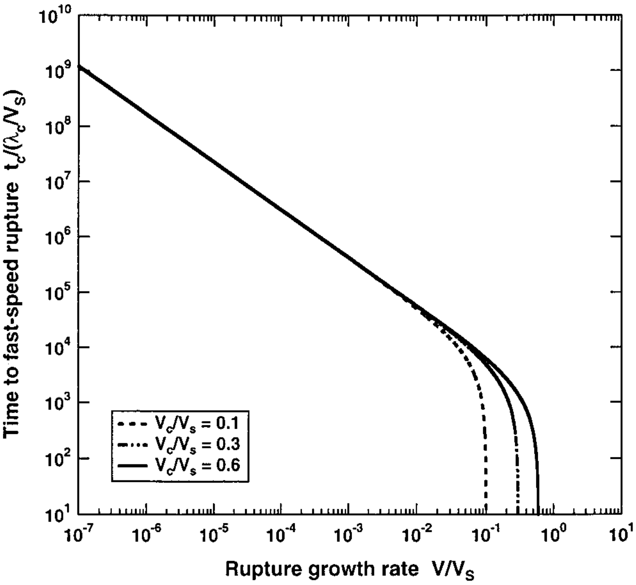

Figure 30. A log-log plot of the dimensionless critical time $t_c/(\lambda_c/V_S) = f(V/V_S, V_c/V_S)$ against the rupture growth rate V normalized to the shear wave velocity V_S.

In Figure 30 the dimensionless critical time $t_c/(\lambda_c/V_S) = f(V/V_S, V_c/V_S)$ is plotted as a function of the dimensionless velocity V/V_S for three cases where the parameter V_c takes a different value of $0.1V_S$, $0.3V_S$, and $0.6V_S$. In this plot the experimentally determined values of $\alpha = 8.87 \times 10^{-29}$ and $n = 7.31$ have been employed. We find from Figure 30 that the time t_c from a stage of any V/V_S in phase II to the critical stage V_c/V_S virtually does not depend on the velocity V_c, except for $V/V_S > 2 \times 10^{-2}$. This shows that t_c is predictable from the relations (21) and (22) (see also Figure 30). For instance, t_c from a stage $V/V_S = 10^{-5}$ in phase II to the critical stage V_c/V_S is 80 ms for the extremely smooth fault ($\lambda_c = 10$ μm), and 1.6 s for the rough fault ($\lambda_c = 200$ μm) of laboratory scale. In contrast, for major earthquakes for which $\lambda_c = 0.1–1$ m has been inferred, t_c from $V/V_S = 10^{-5}$ to the critical stage is of the order of 10 min to 2 hours, and t_c from $V/V_S = 10^{-6}$ to the critical stage is of the order of 1.7–17 hours. These estimates show how the sizes of the nucleation and breakdown zones of shear rupture and their durations are affected by geometric irregularity of the rupturing surfaces.

6. Discussion: Scaling of Scale-Dependent Physical Quantities Up to Large Earthquakes

There are two types of physical quantities inherent in shear rupture: scale-dependent quantities and scale-independent quantities. The scale-dependent quantities include the breakdown zone size X_c and its duration T_c, the nucleation zone size $2L_c$ and its duration t_c, the shear rupture energy G_c, the slip acceleration $\ddot{D}$, and the cutoff frequency $f^s_{\max}$ of the power spectral density of the slip acceleration versus time record observed at a position on the fault, while the scale-independent quantities include the peak shear strength τ_p and the residual friction stress τ_r in the breakdown zone, the breakdown stress drop $\Delta\tau_b$ (defined as the stress difference between τ_p and τ_r), and the slip velocity $\dot{D}$ on the fault [*Ohnaka et al.*, 1987b, 1997; *Ohnaka*, 1995, 1996, 1998].

Scale-dependent physical quantities can be treated unifyingly in quantitative terms by formulating the constitutive law for shear rupture as a slip-dependent law so as to meet the physical principles and constraints to be imposed on the law. This leads to the conclusion that the constitutive law for shear rupture should be formulated primarily as a slip-dependent law [*Ohnaka et al.*, 1997; *Ohnaka*, 1998]. The slip-dependent constitutive formulation includes a scaling parameter D_c, which allows one to give a common interpretation for shear rupture of any size scale, from small scale in the laboratory to large scale in the Earth as an earthquake source [*Ohnaka*, 1995, 1996, 1998; *Ohnaka et al.*, 1997]. This will be further discussed below.

It has been shown that both L_c and X_c are directly related to a scale-dependent constitutive parameter D_c, which is prescribed by a characteristic scale λ_c in the slip direction on the rupturing surfaces. This shows that the nucleation zone size $2L_c$ and the breakdown zone size X_c are characteristic distances representing the nucleation and breakdown processes, respectively. It can also be shown that t_c and T_c are related to D_c, and hence t_c and T_c are characteristic times representing the nucleation and breakdown processes, respectively.

In addition to the above scale-dependent quantities, other scale-dependent physical quantities, such as G_c, $\ddot{D}$, and $f^s_{\max}$, are also expressed theoretically in terms of slip-dependent constitutive law parameters including D_c. For instance, it has been shown that G_c is related to the constitutive law parameters $\Delta\tau_b$ and D_c by [*Palmer and Rice*, 1973; *Rice*, 1980; *Ohnaka and Yamashita*, 1989; *Ohnaka et al.*, 1997]

$$G_c = \int_0^{D_c} [\tau(D) - \tau_r]\, dD = \tfrac{1}{2}\Gamma \Delta\tau_b D_c \tag{23}$$

where Γ is a numerical parameter dependent on a specific form of the slip-dependent constitutive relation [*Ohnaka and Yamashita*, 1989]. The slip acceleration is also expressed in terms of $\Delta\tau_b$ and D_c [*Ida*, 1973; *Ohnaka and Yamashita*, 1989]

$$\ddot{D} = \frac{\Gamma^2 \phi''}{\pi^4}\left(\frac{V}{C(V)}\frac{\Delta\tau_b}{\mu}\right)^2 \frac{1}{D_c} \tag{24}$$

where ϕ'' is the nondimensional slip acceleration and $C(V)$ is a known function of the rupture velocity V [*Ohnaka and Yamashita*, 1989]. Similarly, the cutoff frequency $f^s_{\max}$ at the source is expressed as [*Ohnaka and Yamashita*, 1989]

$$f^s_{\max} = \frac{h}{\pi^2}\left(\frac{V}{C(V)}\frac{\Delta\tau_b}{\mu}\right)\frac{1}{D_c} \tag{25}$$

where h is a numerical constant ($\sim$1.876). All these expressions show that scale-dependent physical quantities are commonly related to the scaling parameter D_c. In contrast, scale-independent physical quantities do not depend on D_c. Such a typical example is the slip velocity, which is expressed as [*Ida*, 1973; *Ohnaka and Yamashita*, 1989]

$$\dot{D} = \frac{\Gamma \phi'}{\pi^2}\frac{V}{C(V)}\frac{\Delta\tau_b}{\mu} \tag{26}$$

where ϕ' is the nondimensional slip velocity. Note that both ϕ'' and ϕ' are scale-independent, because they are dimensionless quantities.

We thus find from the above discussion that scale dependency of scale-dependent physical quantities is commonly ascribed to scale dependency of D_c, and therefore the fundamental question for the scale dependency is why D_c is scale-dependent. The answer for this question is simple. An earthquake source is, in general, considered to be shear rupture on a preexisting fault in the seismogenic zone; however, such a preexisting fault itself exhibits geometric irregularities and mechanical inhomogeneities of various scales in the fault zone. Consider, for instance, a specific case where a local patch of high rupture growth resistance (which may be called "asperity") in the fault zone is broken down. D_c is by definition the slip displacement required for the breakdown of the local patch in this case, and a large amount of slip displacement is needed for the breakdown of the patch of geometrically large size, while only a small amount of slip is necessary for the breakdown of the small patch size.

In the present experimental configuration a characteristic scale on the rupturing surfaces was represented by λ_c, which characterizes geometric irregularity of the fault surfaces in the slip direction. This will be a case which may be applied for real earthquake faults. Another likely case may be that a characteristic scale practically governing the breakdown process during earthquake rupture is determined by the geometric size of a representative patch of high rupture growth resistance on the fault (asperity model). As mentioned in section 2, a local patch of high rupture growth resistance will be attained at portions of fault bend or stepover, at interlocking asperities of large size in the fault zone, and/or at portions of adhesion (or cohesion) healed between the mating fault surfaces during the interseismic period. The geometric size of such a local patch of large scale can be a characteristic size representing the fault by which the breakdown process during earthquake rupture is virtually governed. For instance, the fracture energy G_c, and the maximum slip acceleration $\ddot{D}_{\max}$ at an earthquake source are practically represented by G_c and $\ddot{D}_{\max}$ at a local portion of high rupture growth resistance (or asperity) on the fault. This is discussed specifically below.

It has been evaluated for major earthquakes that G_c is 10^6–10^8 J/m^2 [*Aki*, 1979; *Papageorgiou and Aki*, 1983; *Li*, 1987], that $\Delta\tau_b$ is of the order of 1–10^2 MPa [*Papageorgiou and Aki*, 1983; *Ide and Takeo*, 1997], and that D_c is of the order of 0.1–1 m [*Papageorgiou and Aki*, 1983; *Ide and Takeo*, 1997]. In contrast, laboratory experiments show that $G_c = 10^4$–10^5 J/m^2, $\Delta\tau_b =$ 10–10^2 MPa and $D_c \approx 1$ mm for shear fracture of intact granite samples under lithospheric conditions [*Ohnaka et al.*, 1997] and that $G_c =$ 0.1–1 J/m^2, $\Delta\tau_b = 10^{-2}$–1 MPa, and $D_c = 10^{-6}$–10^{-5} m for stick-slip dynamic failure on preexisting faults (of $\lambda_c =$ 10–50 μm) in the present experiments. From these values we find a great difference in G_c between shear fracture of intact rock sample and stick-slip failure on preexisting faults. This difference, however, is simply ascribed to the differences in both $\Delta\tau_b$ and D_c between them; that is, $\Delta\tau_b$ and D_c for shear fracture of intact rock sample are much larger than $\Delta\tau_b$ and D_c for stick-slip failure. We find another great difference in G_c between major earthquakes and shear fracture of intact rock samples; G_c for major earthquakes is 2–3 orders of magnitude higher than G_c for shear fracture of intact rock samples. Since $\Delta\tau_b$ for major earthquakes is of roughly the same orders of magnitude or slightly less than that for fracture of intact rock samples, the difference in G_c is necessarily ascribed to the difference in D_c. In fact, it has been shown [*Ohnaka*, 1998] that D_c for major earthquakes is 2–3 orders of slip amount larger than D_c for shear fracture of intact rock samples.

The fact that $\Delta\tau_b$ for a representative patch (or asperity) on an earthquake fault is as large as that for shear fracture of intact rock samples in the laboratory shows that the fault strength locally equals the strength of intact rock. However, the geometric size of such a local patch on an earthquake fault is much larger than the size of an intact rock sample in the laboratory. This is inferred from the fact that D_c for a local patch of high rupture growth resistance on a major earthquake fault is much larger than D_c for shear fracture of an intact rock sample in the laboratory.

The maximum slip acceleration $\ddot{D}_{max}$ has generally been evaluated to be of the order of 10 m/s^2 ($\sim 1\ g$) for major earthquakes, whereas $\ddot{D}_{max}$ has been measured to be of the order of 10^5 m/s^2 for stick-slip dynamic failure on preexisting faults of laboratory scale [*Ohnaka et al.*, 1987; *Ohnaka and Yamashita*, 1989]. The huge difference in $\ddot{D}_{max}$ between major earthquakes and stick-slip dynamic failure is explained in quantitative terms from the difference in D_c between the two [*Ohnaka et al.*, 1987b; *Ohnaka and Yamashita*, 1989]. The scale dependency of f^s_{max} can similarly be explained quantitatively [see *Ohnaka and Yamashita*, 1989; *Ohnaka*, 1995, 1996]. Thus scale-dependent physical quantities inherent in shear rupture can be scaled consistently in terms of the scale-dependent constitutive law parameter D_c, which is in turn prescribed by λ_c.

7. Conclusions

The principal conclusions are summarized as follows. The present series of high-resolution experiments on propagating shear rupture on preexisting faults with different surface roughnesses led to the conclusive results that the nucleation process consists of two phases (an initial, quasi-static phase (phase I) and a subsequent accelerating phase (phase II)) and that the nucleation process is affected by geometric irregularity or roughness of the rupturing surfaces. In order to detect the nucleation that proceeds in a localized zone with time it is critical to monitor spatial changes of a series of local shear stresses and slip displacements measured in the vicinity of the fault. Although the shear stress along the fault concentrates more at the location where the fault strength is locally higher, shear rupture begins to nucleate around the location where the strength is the lowest on the fault. In phase I the rupture grows at a slow, steady speed, and the rupture growth rate is independent of the rupture growth length. In phase II, in contrast, the rupture develops at accelerating speeds, and the rupture growth rate increases with an increase in the rupture growth length, according to a power law of the expression (9). The critical size $2L_c$ of the nucleation zone and its duration t_c depend greatly on topographic irregularity of the rupturing surfaces, and the experimental and theoretical analyses show that both L_c and t_c scale with a characteristic length λ_c representing topographic irregularity of the rupturing surfaces in the slip direction. The result provides an important implication for predicting the onset of dynamic high-speed rupture because the run-up distance and time are short to attain the fast-speed rupture on smooth fault surfaces and because a long run-up is necessary for reaching the same speed on rough, irregular fault surfaces. The slip-weakening process during nucleation is less stable and more dynamic on a smoother fault. Scale-dependent physical quantities inherent in shear rupture can be treated unifyingly in quantitative terms; that is, scale dependency of scale-dependent physical quantities is commonly ascribed to scale dependency of the slip-dependent constitutive law parameter D_c, which is in turn governed by λ_c. Although λ_c here is defined as a characteristic wavelength representing geometric irregularity of the fault surfaces in the slip direction, such a characteristic size for an actual earthquake may virtually be represented by the geometric size of the largest patch of high rupture growth resistance on the fault. A unified comprehension can thus be provided for shear rupture of any size scale, from small scale in the laboratory to large scale in the Earth as an earthquake source, if the constitutive law for shear rupture is formulated as a slip-dependent law so as to meet the physical principles and constraints to be imposed on the law.

Acknowledgments. We are grateful to Shingo Yoshida for joining in an early stage of the present series of experiments and to the Associate Editor, Didier Sornette, and the following external/internal reviewers, Brian Kilgore, Anita Odedra, and an anonymous reviewer, for reviewing the original manuscript, whose constructive or critical comments were helpful in improving the manuscript.

References

Aki, K., Characterization of barriers on an earthquake fault, *J. Geophys. Res.*, *84*, 6140–6148, 1979.

Aki, K., Asperities, barriers, characteristic earthquakes and strong motion prediction, *J. Geophys. Res.*, *89*, 5867–5872, 1984.

Aki, K., Scale dependence in earthquake phenomena and its relevance to earthquake prediction, *Proc. Natl. Acad. Sci. U.S.A.*, *93*, 3740–3747, 1996.

Atkinson, B. K., Subcritical crack propagation in rocks: Theory, experimental results and applications, *J. Struct. Geol.*, *4*, 41–56, 1982.

Atkinson, B. K., Subcritical crack growth in geological materials, *J. Geophys. Res.*, *89*, 4077–4114, 1984.

Atkinson, B. K., and P. G. Meredith, The theory of subcritical crack growth with applications to minerals and rocks, in *Fracture Mechanics of Rock*, edited by B. K. Atkinson, pp. 111–166, Academic, San Diego, Calif., 1987.

Beroza, G. C., and W. L. Ellsworth, Properties of the seismic nucleation phase, *Tectonophysics*, *261*, 209–227, 1996.

Charles, R. J., Dynamic fatigue of glass, *J. Appl. Phys.*, *29*, 1657–1662, 1958.

Dieterich, J. H., Preseismic fault slip and earthquake prediction, *J. Geophys. Res.*, *83*, 3940–3948, 1978.

Dieterich, J. H., Earthquake nucleation on faults with rate- and state-dependent strength, *Tectonophysics*, *211*, 115–134, 1992.

Dieterich, J. H., and B. Kilgore, Implications of fault constitutive properties for earthquake prediction, *Proc. Natl. Acad. Sci. U.S.A.*, *93*, 3787–3794, 1996.

Dieterich, J. H., D. W. Barber, G. Conrad, and Q. A. Gorton, Preseismic slip in a large scale friction experiment, *Proc. U.S. Symp. Rock Mech.*, *19*, 110–117, 1978.

Ellsworth, W. L., and G. C. Beroza, Seismic evidence for an earthquake nucleation phase, *Science*, *268*, 851–855, 1995.

Ida, Y., The maximum acceleration of seismic ground motion, *Bull. Seismol. Soc. Am.*, *63*, 959–968, 1973.

Ide, S., and M. Takeo, Determination of constitutive relations of fault slip based on seismic wave analysis, *J. Geophys. Res.*, *102*, 27379–27391, 1997.

Kanamori, H., The nature of seismic patterns before large earthquakes, in *Earthquake Prediction: An International Review*, *Maurice Ewing Ser.*, vol. 4, edited by D. W. Simpson and P. G. Richards, pp. 1–19, AGU, Washington, D. C., 1981.

Kanamori, H., and G. S. Stewart, Seismological aspects of the Guatemala earthquake of February 4, 1976, *J. Geophys. Res.*, *83*, 3427–3434, 1978.

Kato, N., and T. Hirasawa, A numerical study on seismic coupling along subduction zones using a laboratory-derived friction law, *Phys. Earth Planet. Inter.*, *102*, 51–68, 1997.

Kato, N., K. Yamamoto, H. Yamamoto, and T. Hirasawa, Strain-rate effect on frictional strength and the slip nucleation process, *Tectonophysics*, *211*, 269–282, 1992.

Knopoff, L., The organization of seismicity on fault networks, *Proc. Natl. Acad. Sci. U.S.A.*, *93*, 3830–3837, 1996.

Kuwahara, Y., M. Ohnaka, K. Yamamoto, and T. Hirasawa, Effects of the fault surface roughness on unstable slip and a scaling law of slip, *Programme Abstr. Annu. Meet. Seismol. Soc. Jpn.*, *2*, 110, 1985.

Kuwahara, Y., M. Ohnaka, K. Yamamoto, and T. Hirasawa, Accelerating process of rupture during stick-slip failure, *Programme Abstr. Annu. Meet. Seismol. Soc. Jpn.*, *2*, 233, 1986.

Li, V. C., Mechanics of shear rupture applied to earthquake zones, in *Fracture Mechanics of Rock*, edited by B. K. Atkinson, pp. 351–428, Academic, San Diego, Calif., 1987.

Matsu'ura, M., and T. Sato, Loading mechanism and scaling relations of large interplate earthquakes, *Tectonophysics*, *277*, 189–198, 1997.

Matsu'ura, M., H. Kataoka, and B. Shibazaki, Slip-dependent friction law and nucleation processes in earthquake rupture, *Tectonophysics*, *211*, 135–148, 1992.

Ohnaka, M., Nonuniformity of crack-growth resistance and breakdown zone near the propagating tip of a shear crack in brittle rock: A model for earthquake nucleation to dynamic rupture, *Can. J. Phys.*, *68*, 1071–1083, 1990.

Ohnaka, M., Earthquake source nucleation: A physical model for short-term precursors, *Tectonophysics*, *211*, 149–178, 1992.

Ohnaka, M., Critical size of the nucleation zone of earthquake rupture inferred from immediate foreshock activity, *J. Phys. Earth*, *41*, 45–56, 1993.

Ohnaka, M., Constitutive equations for shear failure of rocks, in *Theory of Earthquake Premonitory and Fracture Processes*, edited by R. Teisseyre, pp. 26–44, Pol. Sci. Publ. PWN, Warsaw, 1995.

Ohnaka, M., Nonuniformity of the constitutive law parameters for shear rupture and quasistatic nucleation to dynamic rupture: A physical model of earthquake generation processes, *Proc. Natl. Acad. Sci. U.S.A.*, *93*, 3795–3802, 1996.

Ohnaka, M., Earthquake generation processes and earthquake prediction: Implications of the underlying physical law and seismogenic environments, *J. Seismol. Soc. Jpn.*, *Ser. 2*, *50*, suppl., 129–155, 1998.

Ohnaka, M., and Y. Kuwahara, Characteristic features of local breakdown near a crack-tip in the transition zone from nucleation to unstable rupture during stick-slip shear failure, *Tectonophysics*, *175*, 197–220, 1990.

Ohnaka, M., and T. Yamashita, A cohesive zone model for dynamic shear faulting based on experimentally inferred constitutive relation and strong motion source parameters, *J. Geophys. Res.*, *94*, 4089–4104, 1989.

Ohnaka, M., K. Yamamoto, Y. Kuwahara, and T. Hirasawa, Dynamic processes during slip of stick-slip as an earthquake fault model, *J. Seismol. Soc. Jpn.*, *Ser. 2*, *36*, 53–62, 1983.

Ohnaka, M., Y. Kuwahara, K. Yamamoto, and T. Hirasawa, Dynamic breakdown processes and the generating mechanism for high-frequency elastic radiation during stick-slip instabilities, in *Earthquake Source Mechanics*, *Geophys. Monogr. Ser.*, vol. 37, edited by S. Das, J. Boatwright, and C. H. Scholz, pp. 13–24, AGU, Washington, D. C., 1986.

Ohnaka, M., Y. Kuwahara, and K. Yamamoto, Nucleation and propagation processes of stick-slip failure and normal stress dependence of the physical parameters of dynamic slip failure, *Nat. Disaster Sci.*, *9*, 1–21, 1987a.

Ohnaka, M., Y. Kuwahara, and K. Yamamoto, Constitutive relations between dynamic physical parameters near a tip of the propagating slip zone during stick-slip shear failure, *Tectonophysics*, *144*, 109–125, 1987b.

Ohnaka, M., M. Akatsu, H. Mochizuki, A. Odedra, F. Tagashira, and Y. Yamamoto, A constitutive law for the shear failure of rock under lithospheric conditions, *Tectonophysics*, *277*, 1–27, 1997.

Okubo, P. G., and J. H. Dieterich, Effects of physical fault properties on frictional instabilities produced on simulated faults, *J. Geophys. Res.*, *89*, 5817–5827, 1984.

Palmer, A. C., and J. R. Rice, The growth of slip surfaces in the progressive failure of over-consolidated clay, *Proc. R. Soc. London*, *Ser. A*, *332*, 527–548, 1973.

Papageorgiou, A. S., and K. Aki, A specific barrier model for the quantitative description of inhomogeneous faulting and the prediction of strong ground motion, II, Applications of the model, *Bull. Seismol. Soc. Am.*, *73*, 953–978, 1983.

Rice, J. R., The mechanics of earthquake rupture, in *Physics of the Earth's Interior*, edited by A. M. Dziewonski and E. Boschi, pp. 555–649, North-Holland, New York, 1980.

Rice, J. R., and Y. Ben-Zion, Slip complexity in earthquake fault models, *Proc. Natl. Acad. Sci. U.S.A.*, *93*, 3811–3818, 1996.

Romanowicz, B., Strike-slip earthquakes on quasi-vertical transcurrent faults: Inferences for general scaling relations, *Geophys. Res. Lett.*, *19*, 481–484, 1992.

Scholz, C. H., Scaling laws for large earthquakes: consequences for physical models, *Bull. Seismol. Soc. Am.*, *72*, 1–14, 1982.

Scholz, C. H., A reappraisal of large earthquake scaling, *Bull. Seismol. Soc. Am.*, *84*, 215–218, 1994.

Shibazaki, B., and M. Matsu'ura, Transition process from nucleation to high-speed rupture propagation: scaling from stick-slip experiments to natural earthquakes, *Geophys. J. Int.*, *132*, 14–30, 1998.

Sibson, R. H., Roughness at the base of the seismogenic zone: contributing factors, *J. Geophys. Res.*, *89*, 5791–5799, 1984.

Tullis, T. E., Rock friction and its implications for earthquake prediction examined via models of Parkfields earthquakes, *Proc. Natl. Acad. Sci. U.S.A.*, *93*, 3803–3810, 1996.

Yamashita, T., and M. Ohnaka, Nucleation process of unstable rupture in the brittle regime: A theoretical approach based on experimentally inferred relations, *J. Geophys. Res.*, *96*, 8351–8367, 1991.

M. Ohnaka and L. Shen, Earthquake Research Institute, University of Tokyo, Yayoi 1-1-1, Bunkyo-ku, Tokyo 113-0032, Japan. (ohnaka-m@eri.u-tokyo.ac.jp)

(Received March 4, 1998; revised August 11, 1998;
accepted August 28, 1998.)